The state-of-the-art modeling of cosmogenic Cr isotopes produced in lunar rocks compared with existing calculations and measurements

Bailiang Liu[1], Jingnan Guo[1,2], Mikhail I. Dobynde[1], Jia Liu[1,2], Yingnan Zhang[1,2], Liping Qin[1,2]

[1]Deep space Exploration Laboratory/School of Earth and Space Sciences, University of Science and Technology of China, Hefei, PR China
[2]CAS Center for Excellence in Comparative Planetology, USTC, Hefei, PR China

Key Points:

- We simulate the production rate of cosmogenic Cr nuclides in the lunar terrain with a newly validated lunar radiation model
- We compare the contributions of different processes producing Cr isotopes
- We analyze the relationship between $^{54}Cr/^{52}Cr$ and $^{53}Cr/^{52}Cr$ constraining lunar evolution models

Corresponding author: Jingnan Guo, jnguo@ustc.edu.cn

Abstract

The distribution of Cr isotopes provides useful information to trace the source and origin of extraterrestrial samples, but it is usually influenced by high-energy cosmic rays. Since lunar and terrestrial materials have quite similar Cr isotope compositions, distinguishing the effect of cosmic rays in lunar samples is especially important. Those cosmic radiation particles (primary particles) can react with lunar materials, creating many secondary particles. Both primary and secondary particles can produce cosmogenic nuclides on the Moon. Radiation Environment and Dose at the Moon (REDMoon) is a novel GEANT4 Monte-Carlo model built to simulate the interactions of space particles with the lunar surface and subsurface content. Using this model, we simulate the production of cosmogenic Cr isotopes (^{50}Cr,^{52}Cr,^{53}Cr,^{54}Cr) at different depths of lunar surface, and compare the contribution of different reactions generating these nuclides. The results suggest that spallation reactions are the most important process producing cosmogenic Cr isotopes.We also analyze the relationship between ^{53}Cr/^{52}Cr and ^{54}Cr/^{52}Cr predicted by our model and compare it with different Apollo samples. As previously studied, we also find an approximate linear relationship between ε^{53}Cr and ε^{54}Cr (per 10,000 deviation of ^{53}Cr/^{52}Cr and ^{54}Cr/^{52}Cr ratios from the standard). Furthermore, we reveal a change of this linear relationship in different depths of lunar surface. Besides, we investigate how the slopes can be influenced by exposure age and the Fe/Cr ratio. With these additional factors carefully considered, the comparison between our modeled results and the measurements is better than previous studies.

Plain Language Summary

Cosmic rays arriving at the Moon can change the isotopic compositions on the lunar surface including chromium isotopes which can be used to constrain the evolution history of the Moon. Here, we use the state-of-the-art model to simulate the high-energy particles and the chromium isotopes generated in the lunar material by different cosmic ray sources. After including various factors that have been omitted by previous studies, we reach a better agreement between our model prediction and the Apollo lunar samples. Such an improved analysis of the lunar cosmogenic isotopes contributes to a better understanding of the origin of the Moon.

1 Introduction and Motivation

The short-lived radionuclides can provide constraints for models of nucleosynthesis. Because of the short half life, they are also sensitive chronometers and tracers for extraterrestrial samples and evolutionary processes in the early solar system. The ^{53}Mn-^{53}Cr system is a useful tool to study the fine history of early solar system processes, especially for the first 20 million years (Myr) (Lugmair & Shukolyukov, 1998), with the half life of ^{53}Mn being 3.7 Myr (Honda & Imamura, 1971). The nucleosynthetic anomalies are good indicators to identify the source of the materials migrated in the solar system, and this method is widely used in the study of the Moon. In particular, Cr shows large nucleosynthetic anomalies between samples from various sources in the solar system, but lunar and terrestrial samples have a quite similar Cr isotope composition (Qin et al., 2010). The Moon has only a little higher ε^{53}Cr and ε^{54}Cr (per 10,000 deviation of ^{53}Cr/^{52}Cr and ^{54}Cr/^{52}Cr ratios normalized to the ^{50}Cr/^{52}Cr ratio from the NIST SRM 3112a Cr standard) than the standard value according to sample measurements and this has been suggested to be the additional contribution of cosmogenic Cr generated in the lunar soil and rocks (Qin et al., 2010; Mougel et al., 2018).

Since the Moon has neither an atmosphere nor a magnetosphere, it is permanently bombarded by high-energy cosmic rays which are mainly composed of background Galactic Cosmic Rays (GCRs) and sporadic Solar Cosmic Rays (SCRs). SCRs are sometimes also referred as Solar Energetic Particles or SEPs as they are generated during occasional

solar eruptions (R. C. Reedy & Arnold, 1972). In the Earth's vicinity, SCR ions may have a very high flux in the energy range up to 100 MeV/nucleon, while GCR particles have a relatively stable flux over a wider energy range from several MeV/nucleon to more than 100 GeV/nucleon. When these high energy charged-particles reach the Moon (identified as primary particles), they can react with the lunar surface material, producing a large amount of secondary particles, including charge-free neutrons. The primary and secondary particles in the lunar regolith can further induce spallation and neutron capture processes that can significantly alter the $^{53}Cr/^{52}Cr$ and $^{54}Cr/^{52}Cr$ ratios in lunar surface materials. Therefore, it is important to understand, model and quantify these cosmogenic effects.

There have been studies simulating the production of different cosmogenic nuclides in meteorites and in the lunar return samples (Leya, Halliday, & Wieler, 2003; Leya et al., 2021). There is an approximate linear relationship between $\varepsilon^{53}Cr$ and $\varepsilon^{54}Cr$ in lunar samples according to Mougel et al. (2018), but the predicted linear slope from simulations does not agree with the experimental data very well (Leya, Wieler, & Halliday, 2003). This may be because the model only considered the influence of GCRs when calculating cosmogenic Cr isotopes, while we will show in this study that the SCR contribution makes a significant impact at shallow layers of the lunar regolith.

The REDMoon (Radiation Environment and Dose at the Moon) is a particle transport model in the lunar environment built by Dobynde and Guo (2021) based on GEANT4 code (Agostinelli et al., 2003). It can calculate the primary and secondary particle flux of different types on and under the lunar surface. In this work we first use the REDMoon model to derive the proton (both primary and secondary) and neutron (only secondary) flux at different depths of the lunar regolith. Both GCR and SCR primary particles are considered as possible radiation sources for our calculations. Next, Cr, Fe, Mn, Ni in the lunar material are considered as target elements and we simulate the spallation and neutron capture process induced by energetic protons and neutrons (obtained in the previous step) arriving at these targets using the cross sections from the ENDF/B database, Talys 1.95 codes, and INCL v6.29 codes (A. J. Koning et al., 2007; Boudard et al., 2013).

We calculate and analyze the influence of different reactions producing Cr isotopes in lunar surface materials, and derive the $^{53}Cr/^{52}Cr$ and $^{54}Cr/^{52}Cr$ ratios considering various exposure ages. We find that both SCR and GCR particles can alter the $^{53}Cr/^{52}Cr$ and $^{54}Cr/^{52}Cr$ ratios. Within the first few centimeters of the lunar surface, the main contribution comes from SCRs while at deeper layers the GCR-induced process plays a much more important role. Meanwhile, the sample exposure age and Fe/Cr ratio can also affect the relative ratio of Cr isotopes. With various factors carefully considered in our study, the comparison between our modeled results and the Apollo measurements is much better than previous studies.

The paper is organized as following. In Section 2, we introduce the radiation sources reaching the Moon, including the models and spectra of GCRs and SCRs. Section 3 details the methods and models used in our radiation transport simulations and isotope calculations. The REDMoon model is employed first to simulate the primary and secondary particle flux on lunar surface, followed by calculations of energetic particles generating cosmogenic isotopes via different physical processes in the lunar material. Section 4 displays the simulation results of the production rates of ^{53}Mn, the contribution of different radiation sources and physical processes to Cr isotopes, the ^{53}Cr and ^{54}Cr anomaly and their relationship and finally the comparison with measurements.

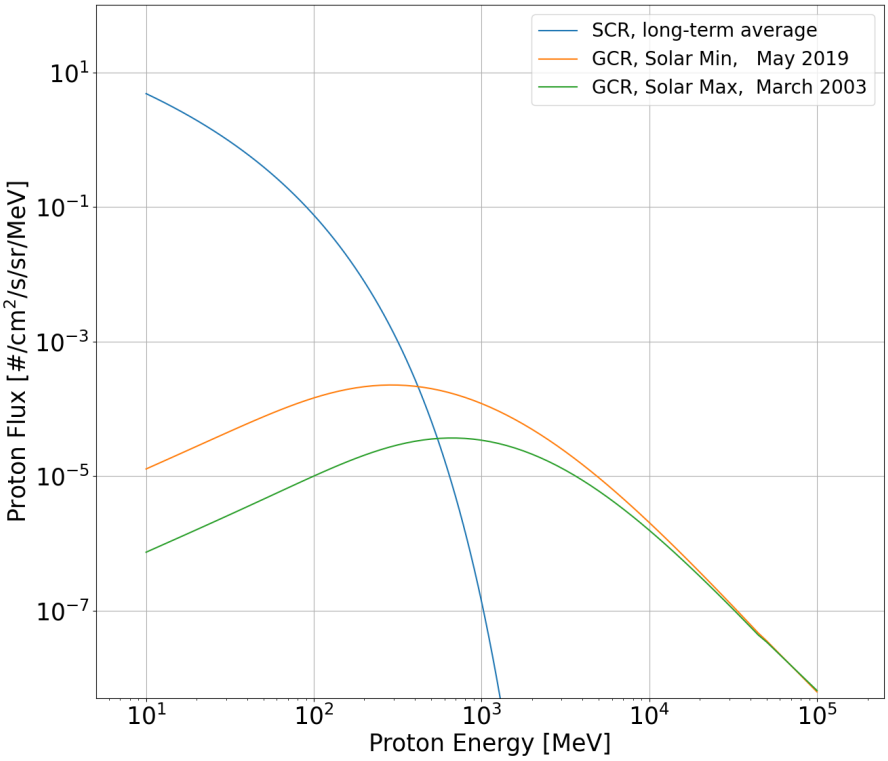

Figure 1. Long-term averaged SCR spectra (see Section 2.2 for details) and GCR proton spectra (see Section 2.1 for details) under different solar activities as shown in the legend.

2 Radiation sources: GCR and SCR sources

2.1 Galactic Cosmic Ray (GCR) Particles

GCRs are energetic charged particles from outside the solar system with a stable flux slowly varying in the long term. At the Earth orbit (1 AU from the Sun), GCR is nearly isotropic, approximately consisting of 87% protons, 12% helium nuclei and ∼1% heavier ions. The GCR flux is modulated by the heliospheric magnetic field as GCRs propagate into the heliosphere (e.g., Potgieter, 2013). A so-called solar modulation potential ϕ is often used to represent the average rigidity loss of a GCR particle in the heliosphere. It thus indicates the strength of the modulation process and is positively correlated with the solar activity cycle, with larger (or smaller) ϕ values during solar maximum (or minimum) years. The value and definition of solar modulation potential ϕ may vary depending on the model describing GCRs. For example, in a widely used GCR model built up by Usoskin et al. (2005), the value of ϕ is based on the modulation potential derived using the count rates of worldwide neutron monitors net. For an other popular model, the Badhwar O'Neill 2014 Galactic Cosmic Ray Flux Model (BON14 O'Neill et al., 2015), ϕ is correlated with the number of sunspots (an indicator of solar activity). The value of ϕ, is also different in that two different models.

In this work we use the BON14 model to predict the GCR flux under different solar activities. The BON14 model accounts for particle transport processes in the heliosphere to derive the GCR spectra by numerically solving the Fokker-Planck differential equation. Such derived flux near the Earth can be calculated and validated against available in-situ particle measurements. The unit of the BON-modeled GCR spectra (derivative of the flux over time and energy) used as input for our work is particles/(MeV/nuc)/cm^2/s.

The GCR proton spectra obtained from the BON14 model under different solar activities are shown in Figure 1. The solar maxima condition shows the monthly average GCR proton spectra in March 2003 and the monthly average ϕ is 1009.5 MV based on BON14, while the solar minima condition is for May 2019 when $\phi = 425$ MV.

Apart from GCR protons, GCR alpha particles and heavy ions up to nickel are all considered as input primary particles arriving at the lunar surface. Their propagation and particle-matter interaction in the lunar regolith is described with REDMoon model to calculate the flux of secondary protons and neutrons.

2.2 Solar Cosmic Ray (SCR) particles

The SCRs are high-energy particles from the Sun. They are mainly protons, electrons, and a small amount of heavier ions. The SCRs normally refer to Solar Energetic Particles (SEPs) which are accelerated during sporadic solar eruptive events and therefore, they have a very unstable flux which can vary greatly over time. However, if we consider the time scales of several solar cycles or the exposure history of an extraterrestrial sample, the long-term average proton flux of SCRs has been estimated (R. C. Reedy & Arnold, 1972; Nishiizumi et al., 2009) as below:

$$\frac{dI}{dR} = k \cdot e^{-\frac{R}{R_0}}. \tag{1}$$

Here I is the proton flux in the unit of particles/cm^2/s; R is the proton rigidity which is $\sqrt{E_p^2 + 2m_pc^2E_p}$, where E_p is the kinetic energy and m_pc^2 is the rest mass of a proton in the unit of MeV. k is a constant in the same unit as I, and R_0 is a fitted spectral parameter, usually ranging from ∼20 to ∼200 MV according to observations (R. Reedy & Nishiizumi, 1998; Nishiizumi et al., 2009). In our model, particle kinetic energies are used and the equation (1) is re-written as a function of energy E_p as:

$$\frac{dI}{dE_p} = g \cdot \frac{E_p + m_pc^2}{\sqrt{E_p^2 + 2m_pc^2E_p}} e^{-\frac{\sqrt{E_p^2+2m_pc^2E_p}}{R_0}} \tag{2}$$

Here g is a constant; the unit of flux dI/dE_p is particles/(MeV/nuc)/cm^2/s, having the same unit as the flux of GCR spectra.

Since the Moon does not have a magnetosphere to guide the direction of incoming charged particles, we consider the long-term averaged SCR flux on the Moon as omnidirectional, similar to the isotropic GCR flux. In this work, when calculating the contribution of SCRs, we only consider SCR protons (R. C. Reedy & Arnold, 1972) using the following parameters: $R_0 = 100$ MV and total proton flux over 10 MeV (which is associated with g and R_0) is 70 protons/cm^2/s following Kohl et al. (1978). The SCR spectrum used in this study is plotted in Figure 1 together with the GCR spectra. It is clearly shown that the SCR flux is much higher than the GCR flux at proton energies below about 500 MeV while the GCR flux extends to a much higher energy range in comparison.

3 Simulation and methods

3.1 The Radiation Environment and Dose at the Moon (REDMoon) model

The REDMoon (Radiation Environment and Dose at the Moon) model (Dobynde & Guo, 2021) is based on the GEANT4 (GEometry ANd Tracking) Monte-Carlo code (Agostinelli et al., 2003), simulating the reaction processes between high-energy particles and the lunar material to derive the radiation environment at the surface and subsurface of the Moon. The lunar geometry is set up as a sphere with a radius of 1737 km (which is the average lunar radius). The lunar surface soil/rock density and element composition is based on the Apollo 17 drill data (McKinney et al., 2006). The GCR/SCR

sources are set to be isotropic arriving at the Moon. All particle interactions with the lunar regolith are tracked down to 10 m beneath the surface of the Moon (as few particles of interest propagate or are generated below this depth). The prediction of REDMoon, especially for albedo neutrons and protons (which are produced secondaries in the lunar soil and get scattered upward to be detected at the surface/orbit of the Moon), has been validated against the measurement results (Dobynde & Guo, 2021; Xu et al., 2022).

With the above setup, REDMoon simulates the flux of both primary and secondary particles in the lunar regolith as a function of injected particles with different type, energy, and angle. REDMoon adopts a so-called response function approach (Dobynde et al., 2021). Each response function is a matrix with each column representing a histogram of secondary particles which are created by primary particles with one certain energy. Secondary particle spectrum can be obtained simply by multiplying the incoming GCR/SCR spectrum with the matrix, rather than running new simulations each time considering a new input particle spectrum. In this work, considering both GCRs (under different ϕ values) and SCRs as input sources , we use REDMoon's response functions to calculate the induced neutron and proton flux at different depths beneath the lunar surface.

3.2 Reactions and cross sections producing cosmogenic isotopes

The main processes producing Cr isotopes in the lunar materials are spallation and neutron capture reactions. In this work we simulate the production of 4 stable cosmogenic Cr isotopes (^{50}Cr, ^{52}Cr, ^{53}Cr, ^{54}Cr), considering four targets elements in the soil: Cr, Fe, Mn, and Ni. The cosmic particles that react with them are neutrons and protons (obtained from the REDMoon model), both of which may induce spallation reactions with the target elements. Besides, neutrons, especially those with energies smaller than 10 keV (thermal and epithermal neutrons), can be captured by Cr isotopes via neutron capture reactions, thus changing the Cr isotope type.

In such calculations, the probability of a certain type of reaction can be represented by the cross section, which is a function of the energy of inject particles (also called an excitation function). We found the excitation function of the four neutron capture reactions which are responsible for Cr isotope generation processes from the Evaluated Nuclear Data File (ENDF/B-VII, Chadwick et al., 2011). These four reactions are: ^{50}Cr(n,g)^{51}Cr, consuming ^{50}Cr; ^{52}Cr(n,g)^{53}Cr, consuming ^{52}Cr while producing ^{53}Cr; ^{53}Cr(n,g)^{54}Cr, consuming ^{53}Cr while producing ^{54}Cr; ^{54}Cr(n,g)^{55}Cr, consuming ^{54}Cr. where n stands for the captured neutron and g stands for the released γ particle. However, there lacks sufficient cross sections based on measurements for spallation reactions we need. Therefore another two models are employed in this work: Talys 1.95 and INCL v6.29. Talys provides reliable cross sections with the injected particles in the energy range from about 1 keV to 200 MeV (A. Koning & Rochman, 2012). Above this energy range, we use ABLA07 (Kelić et al., 2009) as the de-excitation model coupled with INCL v6.29 (Boudard et al., 2013) to derive the cross sections up to 20 GeV.

In additional to direct production of Cr isotopes, there are reactions producing cosmogenic unstable nuclides, which may decay to stable Cr isotopes. For example, ^{53}V and ^{54}V will decay to ^{53}Cr and ^{54}Cr, while ^{53}Ti and ^{54}Ti will decay to ^{53}V and ^{54}V. The cross sections producing such nuclides are independently calculated in Talys 1.95 and INCL v6.29 codes. We consider such cosmogenic unstable nuclides including ^{52}Ti, ^{53}Ti, ^{54}Ti, ^{52}V, ^{53}V, ^{54}V, ^{50}Mn, ^{52}Mn, ^{53}Mn, ^{54}Mn and ^{53}Fe which may finally decay to one of the Cr isotopes (^{50}Cr, ^{52}Cr, ^{53}Cr or ^{54}Cr). Their half-life times are all very short except for ^{53}Mn, whose half-life is $\sim$3.7 million years. Since cosmogenic ^{53}Mn nuclides are continuously decaying and being generated, we must consider the exposure age of lunar samples.

3.3 Production rates of cosmogenic isotopes

We further calculate the production rates $P_i(d)$ of cosmogenic nuclide i via the following equation,

$$P_i(d) = \sum_{q=1}^{Q} N_A \frac{\omega_q}{A_q} \sum_{m=1}^{M} \int_0^{E_{up}} \sigma_{q,m,i}(E) \times J_m(E,d) \times dE. \quad (3)$$

Here d is the column depth of the lunar regolith in the unit of g/cm^2 and it ranges from 0 at the lunar surface to about 550 g/cm^2 (at 3 meters depth). q is the type of target element. Four Cr isotopes are analyzed separately as target nuclides because of the existence of neutron capture reactions, while natural abundances of the Fe, Mn, and Ni isotopes are considered. m is the type of cosmic particle arriving at the target and neutrons and protons (M = 2) are considered as they are the main particles detected in the lunar soil as calculated from the REDMoon model. N_A is the Avogadro constant; A_q is the molar mass of element q and ω_q is the mass percentage of element q in lunar material. $N_A \frac{\omega_q}{A_q}$ gives the number of atoms of element q in lunar material per unit material mass. For a single type of Cr isotope, we use ω_q multiplied by its standard abundance to obtain its number of atoms. $\sigma_{q,m,i}$ is the cross section of the reaction with target q, injecting particle m, and production of nuclide i as a function of injecting particle's energy E. $J_m(E,d)$ is the flux of particle m (neutrons or protons) as a function of energy E and lunar subsurface depth d.

3.4 Derivation of isotope anomalies: ε^{53}Cr and ε^{54}Cr

With the given long-term average GCR and SCR spectra (Section 2.1 and 2.2), the production rate of a specific cosmogenic nuclide is a function of depth as $P_i(d)$. By considering the exposure age of the lunar sample and multiplying it with the production rates, we get the total accumulation of the cosmogenic nuclide in the sample.

We use the Standard Reference Materials (SRM) provided by the National Institute of Standards and Technology (NIST) "NIST SRM 3112a" Cr as the standard value of Cr isotopic abundance. We assume the Cr isotope abundance of lunar samples as the standard value (here we use the NIST SRM 979 value based on Shields et al. (1966) as the input) when they were just exposed to cosmic ray, and consider additional generation of Cr isotopes during their exposure to evaluate the influence of cosmic effect on Cr isotopes. Then we normalize the ^{50}Cr/^{52}Cr ratio to 0.043452/0.837895 (inside 0.051859±0.000100 based on Shields et al. (1966)) using an exponential law, and derive the normalized ^{53}Cr/^{52}Cr ratio and ^{54}Cr/^{52}Cr ratio. Using the normalized ^{53}Cr/^{52}Cr and ^{54}Cr/^{52}Cr, we have the per 10^4 deviation of ^{i}Cr (where i is 53 or 54) as:

$$\varepsilon^i Cr = [\frac{(^iCr/^{52}Cr)_{sample}}{(^iCr/^{52}Cr)_{\text{SRM 3112a}}} - 1] \times 10000 \quad (4)$$

As we have discussed in Section 3.2, cosmic ray will also produce ^{53}Mn which further decays to ^{53}Cr with a half-life of ∼3.7 million years. For lunar samples with an exposure age of 10s Myr or longer, a dynamic equilibrium has been achieved between the production and decay of ^{53}Mn. So when we display the production rates of cosmogenic ^{53}Cr in a figure, it is reasonable to just add the production rate of cosmogenic ^{53}Mn to the directly-produced cosmogenic ^{53}Cr. The same approach is adopted for the other unstable cosmogenic nuclides since their half-lives are all shorter than 1 year. But When further calculating ε^{53}Cr, since cosmogenic ^{53}Mn keeps decaying and generated, we should consider the exact amount of cosmogenic ^{53}Mn atoms which have decayed to ^{53}Cr. The change of ^{53}Mn atoms per kilo of lunar sample with time t is:

$$\frac{dN}{dt} = -\lambda N + P. \quad (5)$$

Here, N is the number of cosmogenic ^{53}Mn atoms in 1 kg lunar material; $\lambda = ln2/\tau$, with τ being the half-life of ^{53}Mn; P is the production rate in the unit of dpm/kg, i.e., the number of atoms produced in 1 kg of sample per minute. As we assumed the long-term average cosmic rays, at a certain depth we consider P as a constant. Let $N = 0$ when the sample was first exposed to cosmic rays, we get:

$$N = \frac{P}{\lambda}(1 - e^{-\lambda t}). \tag{6}$$

With the total amount of ^{53}Mn that have been produced by cosmic rays as $P \cdot t$, the amount decayed to ^{53}Cr is $P \cdot t - N$. Using $(P \cdot t - N)/(P \cdot t)$ to represent the proportion of ^{53}Mn decaying to ^{53}Cr during time t, we get:

$$\frac{P \cdot t - N}{P \cdot t} = 1 - \frac{\tau}{t \cdot ln2}(1 - e^{-\frac{t \cdot ln2}{\tau}}) \tag{7}$$

Let $\tau = 3.7$ Myr, for the exposure age of 25 Myr the proportion is ∼78.8% while for 100 Myr it is ∼94.7%. Since the contribution of cosmogenic ^{53}Mn is quite large to the production of cosmogenic ^{53}Cr (see discussions in Section 4.2), when calculating ε^{53}Cr, we should consider the exact amount of cosmogenic ^{53}Mn atoms which have decayed to ^{53}Cr using equation 7. As for the other unstable cosmogenic nuclides in this work with half-live time shorter than 1 year, we can just think 100 % of them have decayed out.

4 Results

4.1 ^{53}Mn production rates

There lacks experimental results of cosmogenic Cr isotope production rates in lunar samples, but Imamura et al. (1973) measured the cosmogenic ^{53}Mn production rate based on samples from Apollo 15 drill cores. As we have discussed in Section 3.1, although the lunar material in REDMoon model is based on the Apollo 17 drill core, its simulation results such as secondary albedo particles fluxes fit the experimental data well, suggesting that REDMoon can give a reliable prediction of the lunar radiation environment. Such a result can be seen as an average radiation environment in lunar rocks. Figure 2 (a) shows the production rate of ^{53}Mn in 1 kg Fe in lunar samples as a function of depth (in the unit of g/cm^2, which also means the column mass) caused by GCR fluxes under different solar modulation potential ϕ values. The orange squares and green diamonds are experimental data based on Imamura et al. (1973). According to our simulation results, when ϕ is 600 MV (yellow curve), it best fits the experimental data in the soil deeper than 100 g/cm^2, but underestimates the production rates at the first two experimental points (60 and 64 g/cm^2). Therefore we chose 480 MV as a long-term average solar modulation potential, where the simulation results (azure line) are within the error range of most experimental data points. As discussed in Section 3.2 and 3.4, there are cosmogenic ^{53}Fe nuclides decaying to ^{53}Mn with a very short half-life, and it is already taken into account when calculating the production of cosmogenic ^{53}Mn in Figure 2 (a) and (b).

Figure 2 (b) shows the total production rates of ^{53}Mn in 1 kg of lunar Fe material as a function of depth, considering both SCRs ($R_0 = 100$ MV and total proton flux over 10 MeV is 70 protons/cm^2/s based on Kohl et al. (1978)) and GCRs ($\phi = 480$ MV). The experimental data of ^{53}Mn production rate is from Imamura et al. (1973) based on various different lunar samples, and more data for lunar samples with thin shielding are added comparing to Figure 2 (a). The inset at the top right is a zoom-in of the data at shallow depths to better show the details. It is shown that overall our modeled results can fit the experimental data very well confirming the reliability of our model. Comparing Figures 2 (a) and (b), we show that SCRs (not included in Figure 2 (a)) play an important role at shallow depths.

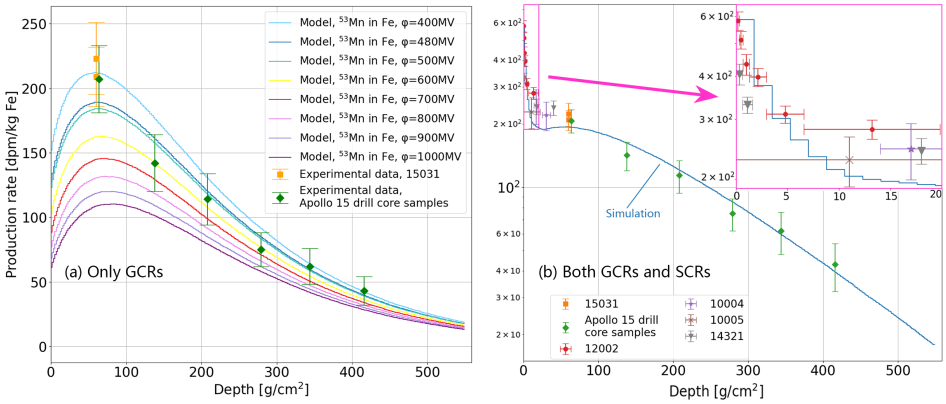

Figure 2. The production rates of ^{53}Mn in 1 kg of lunar iron material as a function of lunar surface depth. Panel (a) shows the effect of only GCRs, while panel (b) shows the result considering both GCRs and SCRs. In panel (a), the curves with different colors are the modeled production rates under different solar modulation potentials, while the points are the experimental data according to lunar rock 15031 and Apollo 15 drill core samples. In panel (b), the solar modulation potential of GCRs is set to 480 MV, and the points in different colors are experimental data. The results of some rocks with shallow shielding are added in panel (b), and the details are shown in the zoomed-in inset at the top right.

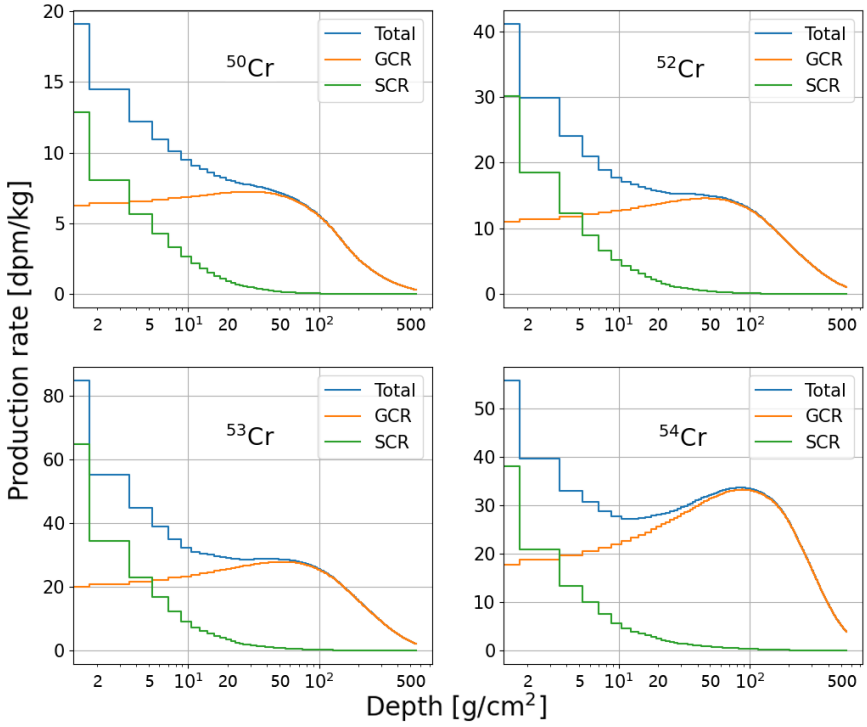

Figure 3. Production rates of Cr isotopes caused by GCRs and SCRs as a function of depth. The results of ^{50}Cr, ^{52}Cr, ^{53}Cr, ^{54}Cr are shown in separate panels. Blue curves are total production rates, while the SCRs and GCRs- related rates are shown in green and orange. The depth is shown along X-axes in g/cm^2 in logarithmic scale.

4.2 Production rates of Cr isotopes

Figure 3 shows the production rates of 4 Cr isotopes caused by both SCRs and GCRs (modulation potential $\phi = 480$ MV). The element content of the lunar regolith in the calculation is based on Apollo 17 drill data. Cr production rates associated with SCRs and GCRs are displayed separately, and the depth (X-axes, in the unit of g/cm^2) is in logarithmic scale. The influence of SCRs is high in shallow layer of the lunar regolith, may higher than the GCR contribution within the depth of $\sim$5 g/cm^2 (approximate 3 cm), but decays very quickly with depth. We consider that it should not be ignored within 15 g/cm^2 of soil depth, and their influence is almost zero for depth deeper than 50 g/cm^2.

Figure 4 shows the respective contribution of spallation and neutron capture reactions to the production of ^{53}Cr and ^{54}Cr. The blue curves stand for spallation reactions, while the red curves represent the net result of neutron capture reactions. As many spallation reactions are taken into consideration, we do not plot each of them separately. As for neutron capture reactions, as we discussed in Section 3.2, we consider 4 reactions, among of which 3 contribute to the generation and consumption of ^{53}Cr and ^{54}Cr isotopes and thus are displayed in Figure 4. The pink curve in the left panel shows the production rate of ^{53}Cr isotope from reaction ^{52}Cr(n,g)^{53}Cr; the purple curves in both panels are for reaction ^{53}Cr(n,g)^{54}Cr; and the green curve in the right panel is for ^{54}Cr(n,g)^{55}Cr. The net contribution of neutron capture reactions to the production of ^{53}Cr is negative, because for neutron capture reactions the consumption of ^{53}Cr is larger than the generation of ^{53}Cr. For the production of ^{54}Cr, the influence of reaction ^{54}Cr(n,g)^{55}Cr consuming ^{54}Cr is very small (the green curve is close to zero across all depths and the red curve is behind the purple curve).

As we have discussed in Section 3.2 and 3.4, there are cosmogenic unstable nuclides decaying to Cr isotopes, increasing the Cr isotope abundance indirectly. All of them except for ^{53}Mn have a very short half-life time, so we think all of them have decayed out. The yellow curve named "Decayed from cosmogenic ^{53}Mn" in Figure 4 (left panel) is in fact the total production rate of cosmogenic ^{53}Mn (including those decayed from cosmogenic ^{53}Fe). All cosmogenic ^{53}Mn is produced by spallation reactions, and it is obvious that ^{53}Mn plays an important role in producing cosmogenic ^{53}Cr comparing the yellow curve to the blue curve.

Our model suggests that the dominant process controlling the cosmogenic Cr isotope of the lunar surface composition are spallation reactions rather than neutron capture reactions. Alternatively, Mougel et al. (2018) suggested neutron capture reaction is the main process because of the correlation between ε^{53}Cr (or ε^{54}Cr) and ^{150}Sm/^{152}Sm ratios, since ^{149}Sm has very large neutron capture cross sections. However, in fact, ^{150}Sm/^{152}Sm ratios can only reflect the flux of low-energy neutrons. From the results of our REDMoon models, the low-energy neutron flux and high-energy neutron flux are closely and positively correlated. Low-energy neutrons can be captured contributing the neutron-capture reactions, while high-energy neutrons can induce spallation reactions. Thus both neutron-capture and spallation reactions could be important due to the large abundance of neutrons across all energy ranges in the lunar soil, and the quantification of their relative contribution needs careful model assessments as we have shown in Figure 4.

4.3 The relationship of ε^{54}Cr and ε^{53}Cr

To calculate the isotope anomaly using the production rates, we assume the cosmic-ray exposure age as 100 Myr and set the soil element content based on Apollo 17 drill. Then the simulated ^{50}Cr/^{52}Cr ratios considering cosmic-ray effect are normalized to the standard value in order to derive ε^{53}Cr and ε^{54}Cr (see Section 3.4). Figure 5 (a) shows the relationship between ε^{54}Cr and ε^{53}Cr produced by GCRs only, and panel (b) shows the results considering both GCRs and SCRs. Markers show calculated data at different depths which are shown with the color.

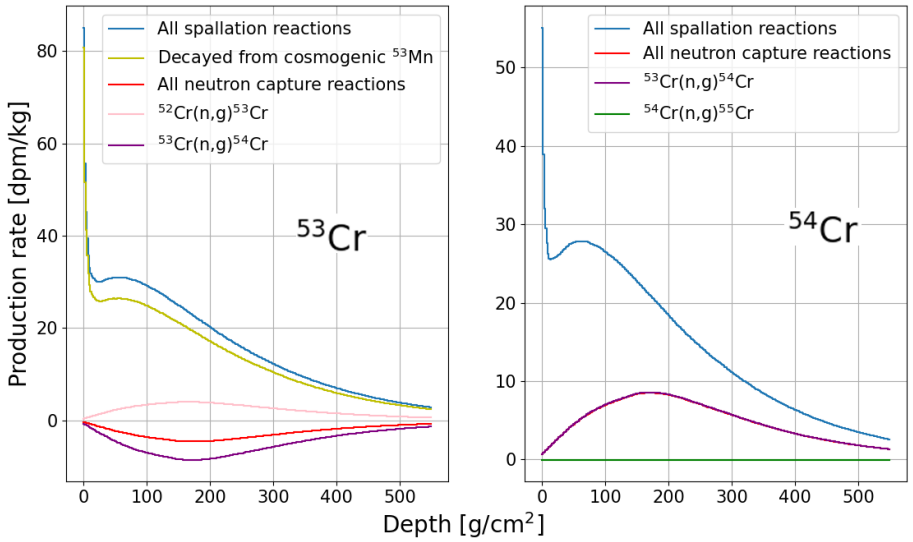

Figure 4. Production rates of spallation and neutron capture reactions producing cosmogenic ^{53}Cr (left) and ^{54}Cr (right) isotopes. The blue and red curves show the respective contribution of spallation and different neutron capture reactions. The yellow curve shows the production rate of cosmogenic ^{53}Mn decaying to ^{53}Cr. The pink, purple, and green curves show different neutron capture reactions according to the legend.

However, the linear fits shown in Figure 5 (b) of all depths are not so good. But we notice that there is a better linear relationship between ε^{54}Cr and ε^{53}Cr at the shallow depth represented by the first several blue points. As stated in Section 4.2, lunar material could be greatly effected by SCRs at shallow layers beneath the surface, while at deeper layers the main contribution is by GCRs. If we separate these two parts, as the red and blue lines/shadow areas displayed in Figure 5(b), there is a clear linear relationship between ε^{54}Cr and ε^{53}Cr in the shallow section (< 15 g/cm^2) where the influence of SCRs cannot be ignored. We fit the slope to be $\sim$2.27 in this part and the result is more consistent with the previous measurements. According to Mougel et al. (2018), there is a good linear relationship between ε^{54}Cr and ε^{53}Cr and the slope is $\sim$2.62 as derived from various lunar samples. The previous calculations which only considered the contribution of GCRs has a fitted slope of $\sim$5.85 (Leya, Wieler, & Halliday, 2003).

Comparing with the measurements (Mougel et al., 2018), our results suggest that the contributions by SCRs at shallow layers are important. This is because of the difference between SCR and GCR fluxes and energy ranges. SCRs have a high flux at low-energy ranges mostly below a few hundred MeVs while GCRs have an extended distribution over a larger energy range up to 10s of GeVs and above. Particles with low energies are more easily stopped by shielding while those with higher energies can penetrate deeper. Therefore, with thin shielding of lunar materials, most cosmogenic nuclides are produced by SCRs at the shallow layers while their contribution is negligible compared to GCRs at deeper layers.

Moreover, we find that the relationship between ε^{53}Cr and ε^{54}Cr is also controlled by the exposure age and the Fe/Cr ratio of the sample. Figure 6 shows evolution of the slopes in shallow (panel a) and inner layers (panel b) change with exposure age (different curve colors) and Fe/Cr ratios (x-axes). The Pearson Correlation Coefficient (PCC) is also plotted which shows that the linear relationship of ε^{53}Cr and ε^{54}Cr with the depth

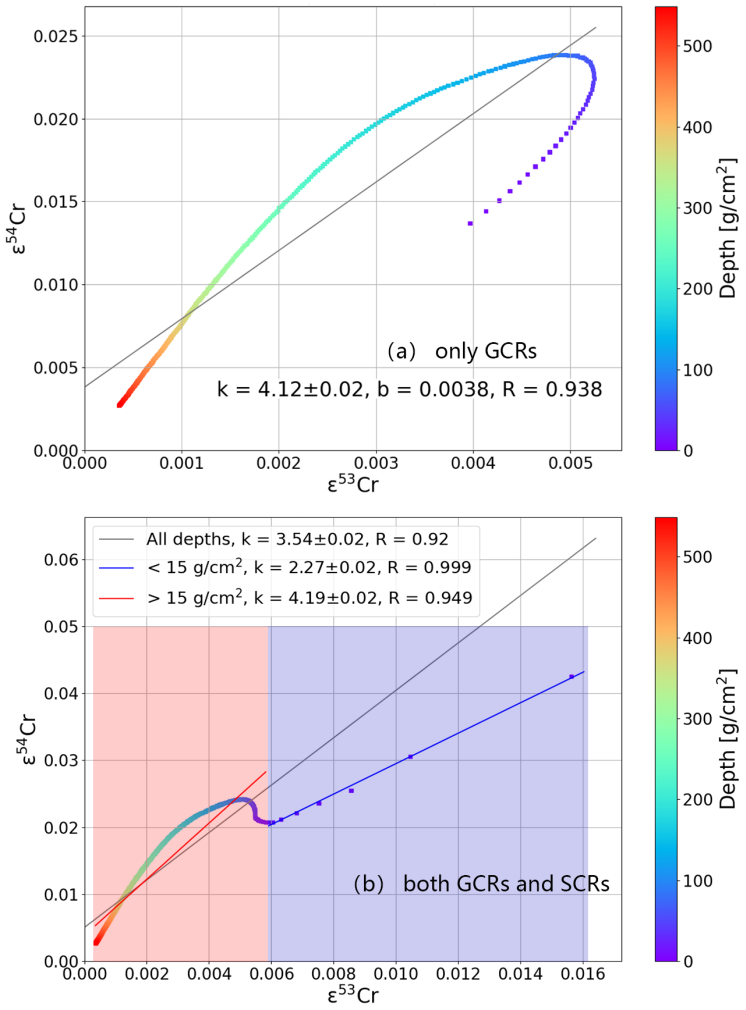

Figure 5. The relationship of ε^{53}Cr and ε^{54}Cr. Different points represent results at different depths starting from purple for shallow depth towards red for deep layers as shown in the color-bar. Panel (a) displays the modeled result considering only GCRs. The gray line shows the linear regression of ε^{54}Cr versus ε^{53}Cr. Panel (b) shows the effect of both GCRs and SCRs. The linear fitting is performed for three regions: at shallow depth (< 15 g/cm^2, blue shadow area, fitted by the blue line), deeper depth (> 15 g/cm^2, red shadow area, fitted by the red line), and the whole depth range (fitted by the gray line). The fitted parameters are given in the legend.

< 15 g/cm^2 (panel a) is always good (PCC>0.997), while this linear relationship becomes weaker at deeper layers. This agrees with the feature shown in Figure 5 (b).

As discussed in Section 3.4, the sample exposure age determines the portion of cosmogenic ^{53}Mn decaying to ^{53}Cr, which is a very important process to produce cosmogenic ^{53}Cr according to Section 4.2. When the exposure age get larger, the portion of cosmogenic ^{53}Mn decaying to ^{53}Cr also increases, leading to a relatively high ε^{53}Cr and a small slope between ε^{53}Cr and ε^{54}Cr. We note that the difference between 25 Myr and 50 Myr is larger than that between 100 Myr and 500 Myr. The reason is that with a 100 Myr of exposure age ~94.7% of cosmogenic ^{53}Mn has already decayed to be ^{53}Cr, and this result will stay almost the same (close to 100%) for a longer exposure age.

As shown, the Fe/Cr ratio of the sample also influences the slope and the influence depends on both the exposure age and the sample depth. This is because the Fe content in lunar rocks is generally high, and spallation reactions with target Fe play an important role in producing cosmogenic Cr isotopes. When the Fe/Cr ratio gets larger, those spallation reactions can have a greater impact to Cr isotope abundance, and the influence of neutron capture reactions decrease relatively.

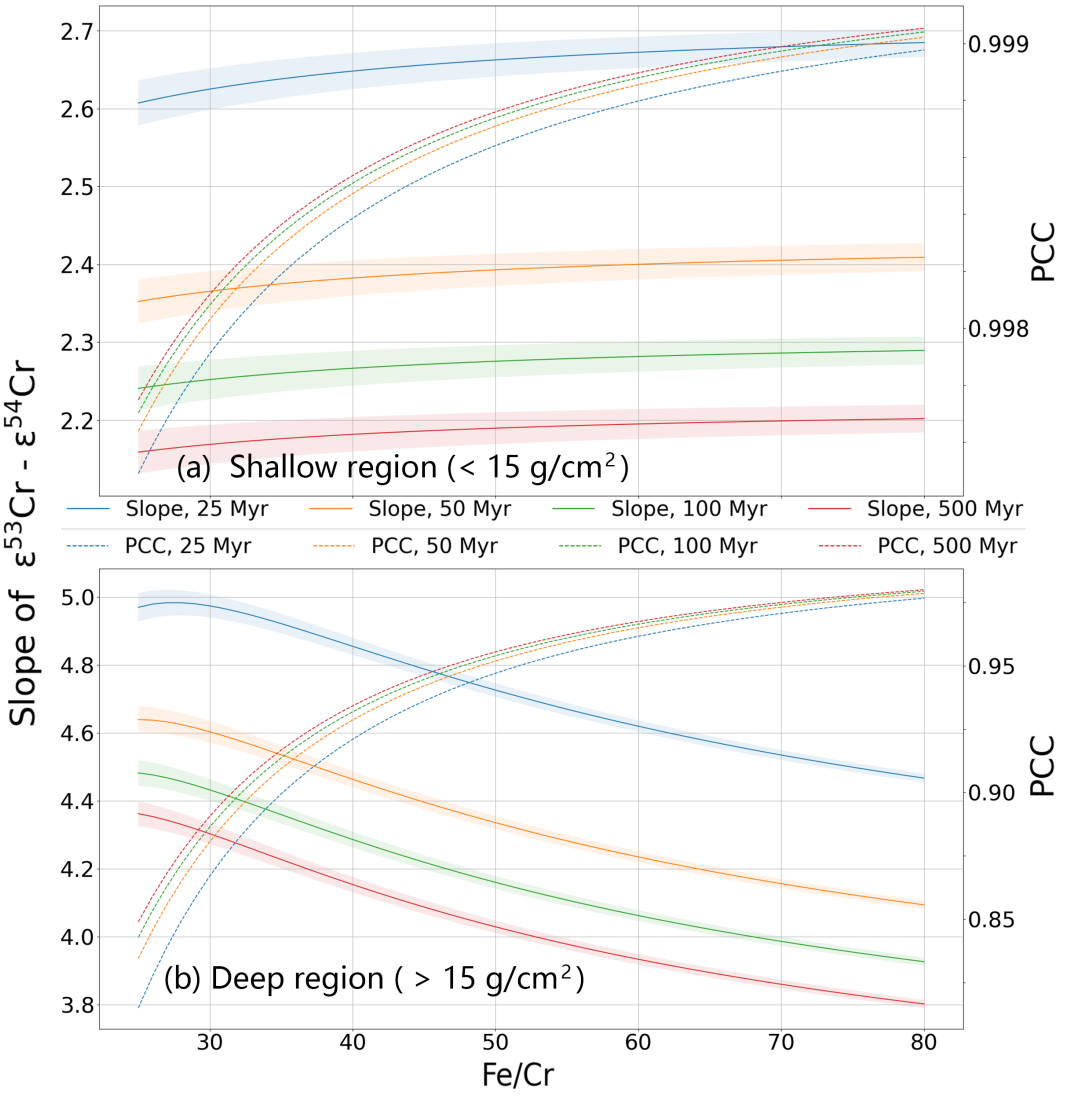

Figure 6. The slope of the fitted linear relationship between ε^{53}Cr and ε^{54}Cr and its dependence on exposure age (different colors) and Fe/Cr ratio (x-axes). The shaded area shows the uncertainty of the fitting. Panel (a) shows the results with the column mass less than 15 g/cm^2 and panel (b) shows layers with larger column mass. Solid curves in different colors represent the slope with the exposure age of 25 Myr (blue line), 50 Myr (orange), 100 Myr (green) and 500 Myr (red), while the shadow areas are the uncertainties of slopes. The dashed curves are the PCC (Pearson correlation coefficient) of different exposure ages, using the same color.

Figure 7 shows the comparison between simulation results and data obtained using Apollo samples (Mougel et al., 2018; Qin et al., 2010), and the references providing

the exposure ages are shown in Table 1. Ten samples with their respective uncertainties (green points) are marked in separate panels and the exposure age and Fe/Cr ratio of each are shown in the legend. Each panel also plots the ε^{53}Cr and ε^{54}Cr values at different depth predicted by our model considering the exposure age and Fe/Cr ratio of the corresponding sample. The correlation of ε^{54}Cr versus ε^{53}Cr at shallow (shown with purple markers) and inner layers (orange markers) are fitted by a linear slope in each region, respectively.

The original depth of samples used here is unknown. However, our model can be used to give some indications. As shown in Figure 7, the modeled relationship between ε^{53}Cr and ε^{54}Cr within the depth of 15 g/cm^2 (blue curves) match with most of the experimental data (green markers with errorbars), suggesting that these samples are for near-surface layers with small regolith shielding. Among those 10 samples, three (12005, 12016 and 12063) are measured by Rancitelli et al. (1971) to obtain the production rates of ^{54}Mn. We compare our simulation results of ^{54}Mn with the measured production rates and derive the sample depth. As shown in Figure 8, the blue curves give the depth-dependent ^{54}Mn production rates, while the orange horizontal lines show the measurement results. Their intersections can be used to derive the depth which is marked by the vertical red lines. All three samples are located at a depth smaller than 10 g/cm^2.

According to Section 4.1 (see, e.g., Figure 2), our simulation results of the production rates of cosmogenic isotopes can fit the measurements well. Nevertheless, we note that the values of modeled ε^{53}Cr and ε^{54}Cr are mostly below experimental results. This suggests that there may be other influencing factors generating Cr isotope anomaly rather than cosmic rays.

Table 1. Exposure age database in Figure 7

Lunar sample	Exposure age/Myr	Reference
12002	144	D'Amico et al. (1971)
12040	285	Burnett et al. (1975)
12063	140	Burnett et al. (1975)
15555	81	Marti and Lightner (1972)
70017	220	Phinney et al. (1975)
77215	27.2	Stettler et al. (1974)

5 Summary and Discussion

By comparing the production rates from different reactions (Section 4.2), we suggest that the main processes producing cosmogenic Cr isotopes are spallation reactions, rather than neutron capture reactions which were suggested by previous studies (Mougel et al., 2018). In that work neutron capture reactions are thought to be the main process producing Cr because of the correlation between ε^{53}Cr (or ε^{54}Cr) and ^{150}Sm/^{152}Sm ratios. Cosmogenic ^{150}Sm is mostly produced by neutron capture reactions because of the large cross sections of neutron capture reaction ^{149}Sm(n,g)^{150}Sm. Thus, the production of ^{150}Sm directly reflects the flux of secondary neutrons in the lunar material. Alternatively, for production of Cr isotopes, the process is not the same because the cross sections of neutron capture reactions producing Cr isotopes are not so large compared to the Sm isotpoes. The production of Cr isotopes significantly depends on the neutron flux, and neutrons can not only be captured, but also induce spallation reactions. We also note that most of the cosmogenic ^{53}Cr are decayed from cosmogenic ^{53}Mn (which

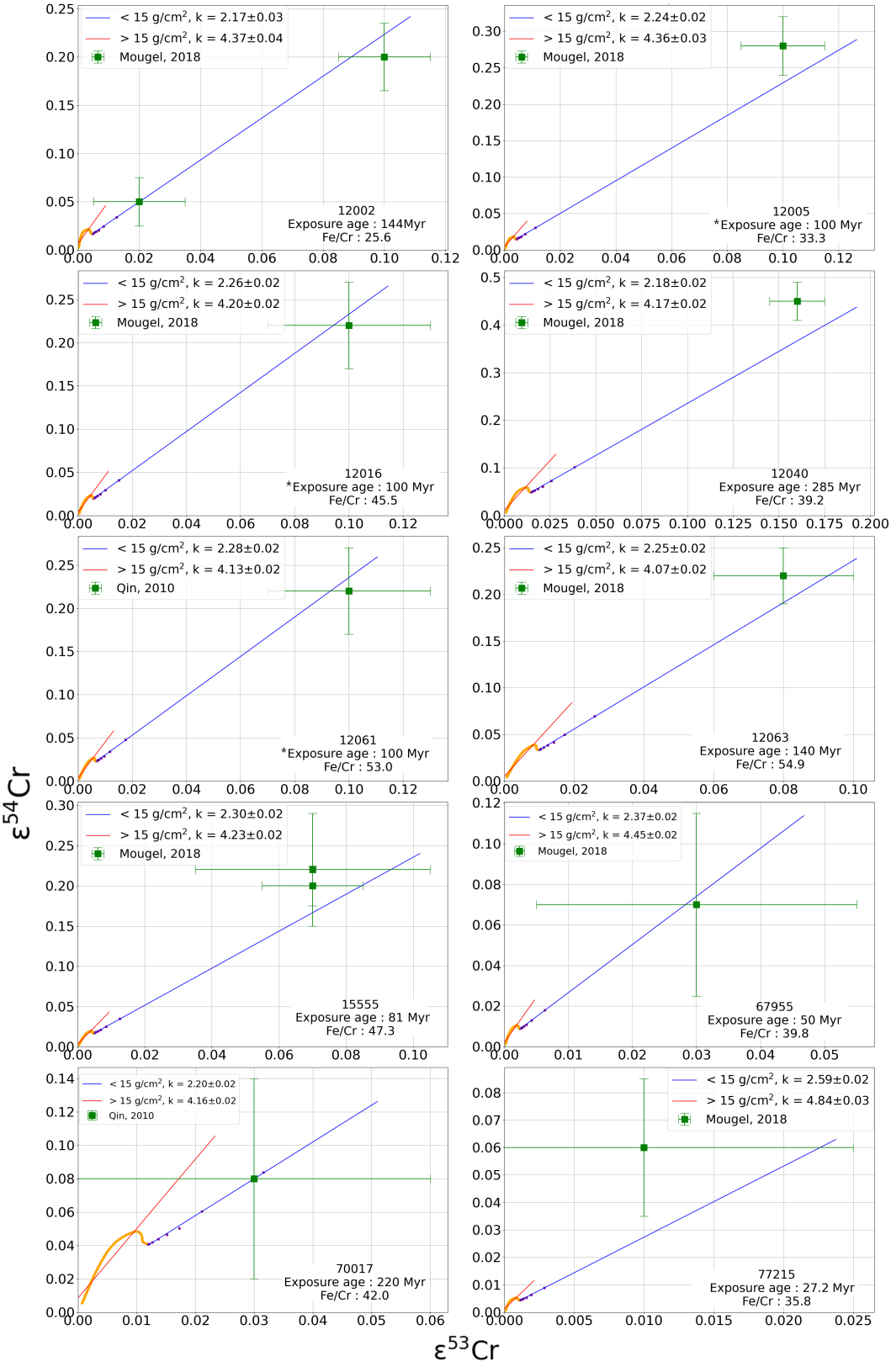

Figure 7. The simulation results and the experimental data for lunar rocks. Purple points are simulation results with depth < 15 g/cm^2, and orange points are in deeper sections. The blue and red curves show the linear regression between ε^{53}Cr and ε^{54}Cr in those two depth ranges (above 15 g/cm^2 and below 15 g/cm^2) separately. Green points are experimental data. If there is no exposure age data for a sample, we assume it as 100 Myr, and mark it with * in the figure.

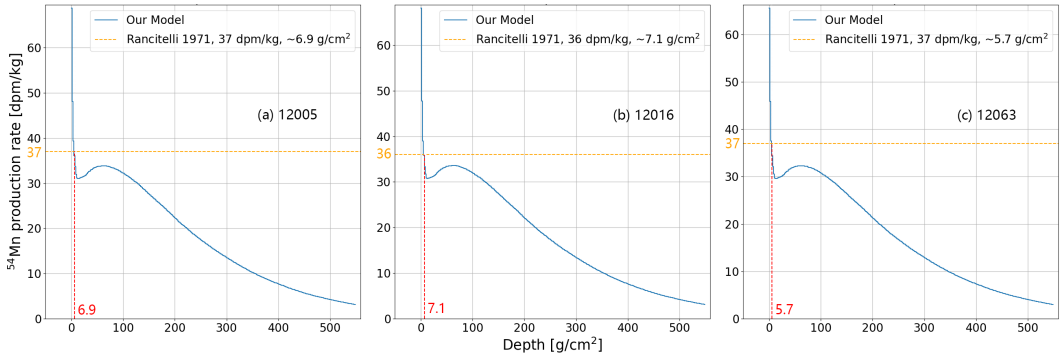

Figure 8. The production rate of ^{54}Mn inside 12005,12016 and 12063, and the change of ^{54}Mn production rates with depth in our model (blue lines). The experimental production rates were pointed out by horizontal orange dashed curves and the fitted depth are located by the vertical red dashed lines.

is produced via spallation process), and the neutron capture reaction can even reduce ^{53}Cr because of the larger cross section of reaction ^{53}Cr(n,g)^{54}Cr compared to ^{52}Cr(n,g)^{53}Cr.

The total production rates in our model fit the experimental data well (Imamura et al., 1973) as shown in Figure 2. As shown in Section 3.4, by considering both the production rates and exposure ages, we calculate the amount of cosmogenic Cr isotopes that have been accumulated during that time. In order to simulate the isotope anomaly caused by cosmic ray effect alone, we assume the Cr isotope abundance of lunar samples as the standard value when they started being exposed to cosmic ray. However, the values of simulated ε^{53}Cr and ε^{54}Cr are mostly lower than experimental results, as shown in Figure 7. Such results suggest that cosmogenic Cr isotopes do influence the Cr isotope abundance on the Moon, but it may not be the only reason.

As for the relationship between ε^{53}Cr and ε^{54}Cr, in Section 4.3 we compare our modeled results with the previous experimental data which have been influenced by various factors and uncertainties such as the sample depth, exposure age, and the Fe/Cr ratio. Therefore, we also include these factors specifically for modeling each sample. There has been found a good linear relationship between measured ε^{53}Cr and ε^{54}Cr, and the experimental slope is ∼2.62 (Mougel et al., 2018; Qin et al., 2010). However, for the first time we found that the slopes are different in two different depth ranges where shallow layer is influenced by both SCRs and GCRs while inner layers have negligible influence by SCRs. By comparing the fitted slope of modeled results at different depth ranges with the experimental data, we suggest that the aforementioned lunar samples are from shallow layer. In this depth range, if the sample has an exposure age long enough (not shorter than 25 Myr) and a Fe/Cr ratio not lower than 20, there is always a good linear relationship and a stable slope value derived from the modeled results (see Figure 6 (a)).

There also remain several problems in our work. First, the slope of ε^{54}Cr versus ε^{53}Cr is modeled to be 2.27 (Fig. 5, which is close to the experimental result (∼ 2.62) compared to previous studies (∼ 5.85, by Leya, Wieler, and Halliday (2003)). However, it is still a little lower.

Second, the samples we considered in Figure 7 are all lunar rocks which have solid shape and different self shielding at different depth. Alternatively, our model considers the lunar surface regolith as the only shielding and does not account for the rock self-shielding. Future considerations of measurement based on lunar soil samples at different subsurface depth may be more appropriate to compare with our models.

Third, our simulation about the relationship between ε^{53}Cr and ε^{54}Cr in samples with very low Fe/Cr ratios and short exposure age is also not accurate. For instance, two lunar rocks with really low Fe content (60015 with FeO content is 0.35%; 62255 with FeO content is 0.2%; both with an exposure age of $\sim$ 2 Myr; results not shown in Figure 7) were also measured by Mougel et al. (2018). But our simulated slopes of that two samples could not fit the data. The exposure age of 2 Myr is too short for our model that most cosmogenic ^{53}Mn do not decay into ^{53}Cr. A very low Fe/Cr ratio in our model can cause a relatively higher impact of neutron capture reactions, consuming more ^{53}Cr (see Section 4.2 and Figure 4). All of that lead to a relatively lower ε^{53}Cr and a much higher slope between ε^{54}Cr and ε^{53}Cr.

Finally, the long-term GCR and SCR spectra should also change with time, and the averaged flux would be different for samples with different exposure ages. However, this effect is rather difficult to address, as the evolution of GCR/SCR spectra over hundreds of Myr time scales is mostly unknown (Usoskin, 2017). So we use the same long-term average spectrum which is determined by the measured ^{53}Mn production rates for all the lunar samples considered. Certainly, given the half-life of ^{53}Mn being only 3.7 Myr, this spectrum may not reflect the average spectra throughout 10s or 100s million years.

6 Conclusion

In this work we calculate the production of Cr isotopes at different depth under the lunar surface. As a novel result, we find that the main processes producing cosmogenic Cr isotopes are the spallation reactions and most of the cosmogenic ^{53}Cr are decayed from cosmogenic ^{53}Mn. Since ^{53}Mn has a half-life of 3.7 Myr and is constantly forming induced by cosmic rays and decaying in the lunar material, the exposure age of the lunar rocks will influence the proportion of cosmogenic ^{53}Mn that decays to cosmogenic ^{53}Cr.

We also find that the relationship between ε^{53}Cr and ε^{54}Cr is determined by the depth (which reflects the influence of different cosmic ray sources), the exposure age, and the Fe/Cr ratio. For the first time, we note that there are two different slopes in two depth ranges, where shallow layers are influenced by both SCRs and GCRs while in the inner layers the impact of SCRs can be ignored. Comparing the modeled and measured results, we further suggest the lunar rocks measured by Mougel et al. (2018); Qin et al. (2010) should be collected from shallow layers. Nevertheless, the value of ε^{53}Cr and ε^{54}Cr from our model is mostly lower than the experimental results, suggesting that the isotope anomaly of ^{53}Cr and ^{54}Cr in lunar samples may be influenced by other factors than cosmic rays which need further investigations in the future.

Acknowledgement

This work is supported by the Strategic Priority Program of the Chinese Academy of Sciences (Grant No. XDB41000000) and the National Natural Science Foundation of China (Grant No. 42074222, 42188101, 41941001).

Data Availability Statement

We acknowledge the models and codes listed below.

The Radiation Environment and Dose at the Moon (REDMoon) model is detailed in Dobynde and Guo (2021), and the resulting data sets are available at `https://doi.org/10.5281/zenodo.5561427`.

The Badhwar O'Neill 2014 Galactic Cosmic Ray Flux (BON14) Model is detailed in O'Neill et al. (2015).

The Talys 1.95 code can be assessed in A. J. Koning et al. (2007) and can be download at the page `https://tendl.web.psi.ch/tendl_2021/talys.html`.

The Liège intranuclear cascade model (INCL) is described by Boudard et al. (2013). It is detailed at the page `https://irfu.cea.fr/dphn/Spallation/incl.html`, and one can request access to the INCL code there.

We also acknowledge the following data source: Experimental Nuclear Reaction Data (EXFOR, `https://www-nds.iaea.org/exfor/`), Evaluated Nuclear Data File (ENDF, `https://www-nds.iaea.org/exfor/endf.htm`).

References

Agostinelli, S., Allison, J., Amako, K., Apostolakis, J., Araujo, H., Arce, P., ... Zschiesche, D. (2003, Jul). Geant4—a simulation toolkit. *Nuclear Instruments and Methods in Physics Research Section A: Accelerators, Spectrometers, Detectors and Associated Equipment*, 250–303. Retrieved from `http://dx.doi.org/10.1016/s0168-9002(03)01368-8` doi: 10.1016/s0168-9002(03)01368-8

Boudard, A., Cugnon, J., David, J.-C., Leray, S., & Mancusi, D. (2013, Jan). New potentialities of the liège intranuclear cascade model for reactions induced by nucleons and light charged particles. *Physical Review C*. Retrieved from `http://dx.doi.org/10.1103/physrevc.87.014606` doi: 10.1103/physrevc.87.014606

Burnett, D., Drozd, R., Morgan, C., & Podosek, F. (1975). Exposure histories of bench crater rocks. In *In: Lunar science conference, 6th, houston, tex., march 17-21, 1975, proceedings. volume 2.(a78-46668 21-91) new york, pergamon press, inc., 1975, p. 2219-2240.* (Vol. 6, pp. 2219–2240).

Chadwick, M., Herman, M., Obložinský, P., Dunn, M., Danon, Y., Kahler, A., ... Young, P. (2011). Endf/b-vii.1 nuclear data for science and technology: Cross sections, covariances, fission product yields and decay data. *Nuclear Data Sheets*, *112*(12), 2887-2996. Retrieved from `https://www.sciencedirect.com/science/article/pii/S009037521100113X` (Special Issue on ENDF/B-VII.1 Library) doi: https://doi.org/10.1016/j.nds.2011.11.002

D'Amico, J., DeFelice, J., Fireman, E., Jones, C., & Spannagel, G. (1971). Tritium and argon radioactivities and their depth variations in apollo 12 samples. In *Proceedings of the lunar science conference, vol. 2, p. 1825* (Vol. 2, p. 1825).

Dobynde, M. I., & Guo, J. (2021, Nov). Radiation environment at the surface and subsurface of the moon: Model development and validation. *Journal of Geophysical Research: Planets*. Retrieved from `http://dx.doi.org/10.1029/2021je006930` doi: 10.1029/2021je006930

Dobynde, M. I., Shprits, Y. Y., Drozdov, A. Y., Hoffman, J., & Li, J. (2021). Beating 1 Sievert: Optimal Radiation Shielding of Astronauts on a Mission to Mars. *Space Weather*, *19*(9), 1–13. doi: 10.1029/2021sw002749

Honda, M., & Imamura, M. (1971). Half-life of mn 53. *Physical Review C*, *4*(4), 1182. Retrieved from `http://dx.doi.org/10.1103/physrevc.4.1182` doi: 10.1103/physrevc.4.1182

Imamura, M., Finkel, R., & Wahlen, M. (1973, Sep). Depth profile of53mn in the lunar surface. *Earth and Planetary Science Letters*, 107–112. Retrieved from `http://dx.doi.org/10.1016/0012-821x(73)90146-5` doi: 10.1016/0012-821x(73)90146-5

Kelić, A., Ricciardi, M., & Schmidt, K.-H. (2009, Jun). Abla07 - towards a complete description of the decay channels of a nuclear system from spontaneous fission to multifragmentation. *arXiv: Nuclear Theory,arXiv: Nuclear Theory*.

Kohl, C., Murrell, M., Russ, G., & Arnold, J. (1978, Jan). Evidence for the constancy of the solar cosmic ray flux over the past ten million years - mn-53

and al-26 measurements. *Lunar and Planetary Science Conference Proceedings,Lunar and Planetary Science Conference Proceedings*.

Koning, A., & Rochman, D. (2012, Dec). Modern nuclear data evaluation with the talys code system. *Nuclear Data Sheets*, 2841–2934. Retrieved from http://dx.doi.org/10.1016/j.nds.2012.11.002 doi: 10.1016/j.nds.2012.11.002

Koning, A. J., Hilaire, S., & Duijvestijn, M. C. (2007, Jan). Talys-1.0. In *Nd2007*. Retrieved from http://dx.doi.org/10.1051/ndata:07767 doi: 10.1051/ndata:07767

Leya, I., Halliday, A. N., & Wieler, R. (2003, Sep). The predictable collateral consequences of nucleosynthesis by spallation reactions in the early solar system. *The Astrophysical Journal*, 605–616. Retrieved from http://dx.doi.org/10.1086/376795 doi: 10.1086/376795

Leya, I., Hirtz, J., & David, J.-C. (2021, Apr). Galactic cosmic rays, cosmic-ray variations, and cosmogenic nuclides in meteorites. *The Astrophysical Journal*, 136. Retrieved from http://dx.doi.org/10.3847/1538-4357/abe52f doi: 10.3847/1538-4357/abe52f

Leya, I., Wieler, R., & Halliday, A. N. (2003, Feb). The influence of cosmic ray production on extinct nuclide systems. *Geochimica et Cosmochimica Acta*, 529–541. Retrieved from http://dx.doi.org/10.1016/s0016-7037(02)01091-8 doi: 10.1016/s0016-7037(02)01091-8

Lugmair, G., & Shukolyukov, A. (1998, Aug). Early solar system timescales according to 53mn-53cr systematics. *Geochimica et Cosmochimica Acta*, 2863–2886. Retrieved from http://dx.doi.org/10.1016/s0016-7037(98)00189-6 doi: 10.1016/s0016-7037(98)00189-6

Marti, K., & Lightner, B. (1972). Rare gas record in the largest apollo 15 rock. *Science*, *175*(4020), 421–422.

McKinney, G. W., Lawrence, D. J., Prettyman, T. H., Elphic, R. C., Feldman, W. C., & Hagerty, J. J. (2006, Jan). Mcnpx benchmark for cosmic ray interactions with the moon. *Journal of Geophysical Research*. Retrieved from http://dx.doi.org/10.1029/2005je002551 doi: 10.1029/2005je002551

Mougel, B., Moynier, F., & Göpel, C. (2018, Jan). Chromium isotopic homogeneity between the moon, the earth, and enstatite chondrites. *Earth and Planetary Science Letters*, 1–8. Retrieved from http://dx.doi.org/10.1016/j.epsl.2017.10.018 doi: 10.1016/j.epsl.2017.10.018

Nishiizumi, K., Arnold, J., Kohl, C., Caffee, M., Masarik, J., & Reedy, R. (2009, Apr). Solar cosmic ray records in lunar rock 64455. *Geochimica et Cosmochimica Acta*, 2163–2176. Retrieved from http://dx.doi.org/10.1016/j.gca.2008.12.021 doi: 10.1016/j.gca.2008.12.021

O'Neill, P., Golge, S., & Slaba, T. (2015, Mar). *Badhwar-o'neill 2014 galactic cosmic ray flux model description* (Tech. Rep.).

Phinney, D., Kahl, S., & Reynolds, J. (1975). /ar-40/-/ar-39/dating of apollo 16 and 17 rocks. In *In: Lunar science conference, 6th, houston, tex., march 17-21, 1975, proceedings. volume 2.(a78-46668 21-91) new york, pergamon press, inc., 1975, p. 1593-1608.* (Vol. 6, pp. 1593–1608).

Potgieter, M. (2013, Jun). Solar modulation of cosmic rays. *Living Reviews in Solar Physics*, *10*. Retrieved from http://dx.doi.org/10.12942/lrsp-2013-3 doi: 10.12942/lrsp-2013-3

Qin, L., Alexander, C. M., Carlson, R. W., Horan, M. F., & Yokoyama, T. (2010, Feb). Contributors to chromium isotope variation of meteorites. *Geochimica et Cosmochimica Acta*, 1122–1145. Retrieved from http://dx.doi.org/10.1016/j.gca.2009.11.005 doi: 10.1016/j.gca.2009.11.005

Rancitelli, L., Perkins, R., Felix, W., & Wogman, N. A. (1971). Erosion and mixing of the lunar surface from cosmogenic and primordial radio-nuclide measurements in apollo 12 lunar samples. In *Proceedings of the lunar science conference, vol. 2, p. 1757* (Vol. 2, p. 1757).

Reedy, R., & Nishiizumi, K. (1998, Mar). Factors affecting the interpretation of solar-proton-produced nuclides and some chlorine-36 results. *Lunar and Planetary Science Conference,Lunar and Planetary Science Conference*.

Reedy, R. C., & Arnold, J. R. (1972, Feb). Interaction of solar and galactic cosmic-ray particles with the moon. *Journal of Geophysical Research*, 537–555. Retrieved from http://dx.doi.org/10.1029/ja077i004p00537 doi: 10.1029/ja077i004p00537

Shields, W. R., Murphy, T. J., Catanzaro, E. J., & Garner, E. L. (1966). Absolute isotopic abundance ratios and the atomic weight of a reference sample of chromium. *Journal of research of the National Bureau of Standards. Section A, Physics and chemistry*, *70*(2), 193.

Stettler, A., Eberhardt, P., Geiss, J., & Grögler, N. (1974). 39ar-40ar ages of samples from the apollo 17 station 7 boulder and implications for its formation. *Earth and Planetary Science Letters*, *23*(3), 453–461.

Usoskin, I. G. (2017). A history of solar activity over millennia. *Living Reviews in Solar Physics*, *14*(1), 3. Retrieved from https://doi.org/10.1007/s41116-017-0006-9 doi: 10.1007/s41116-017-0006-9

Usoskin, I. G., Alanko-Huotari, K., Kovaltsov, G. A., & Mursula, K. (2005, Jan). Heliospheric modulation of cosmic rays: Monthly reconstruction for 1951–2004. *Journal of Geophysical Research*. Retrieved from http://dx.doi.org/10.1029/2005ja011250 doi: 10.1029/2005ja011250

Xu, Z., Guo, J., Wimmer-Schweingruber, R. F., Dobynde, M. I., Kühl, P., Khaksarighiri, S., & Zhang, S. (2022, Sep). Primary and albedo protons detected by the lunar lander neutron and dosimetry (lnd) experiment on the lunar farside. *Frontiers in Astronomy and Space Sciences*, *9*. Retrieved from http://dx.doi.org/10.3389/fspas.2022.974946 doi: 10.3389/fspas.2022.974946

Figure 1.

SCR, long-term average
GCR, Solar Min, May 2019
GCR, Solar Max, March 2003

Proton Flux [#/cm^2/s/sr/MeV]

10^{1}
10^{-1}
10^{-3}
10^{-5}
10^{-7}

10^{1} 10^{2} 10^{3} 10^{4} 10^{5}

Proton Energy [MeV]

Figure 2.

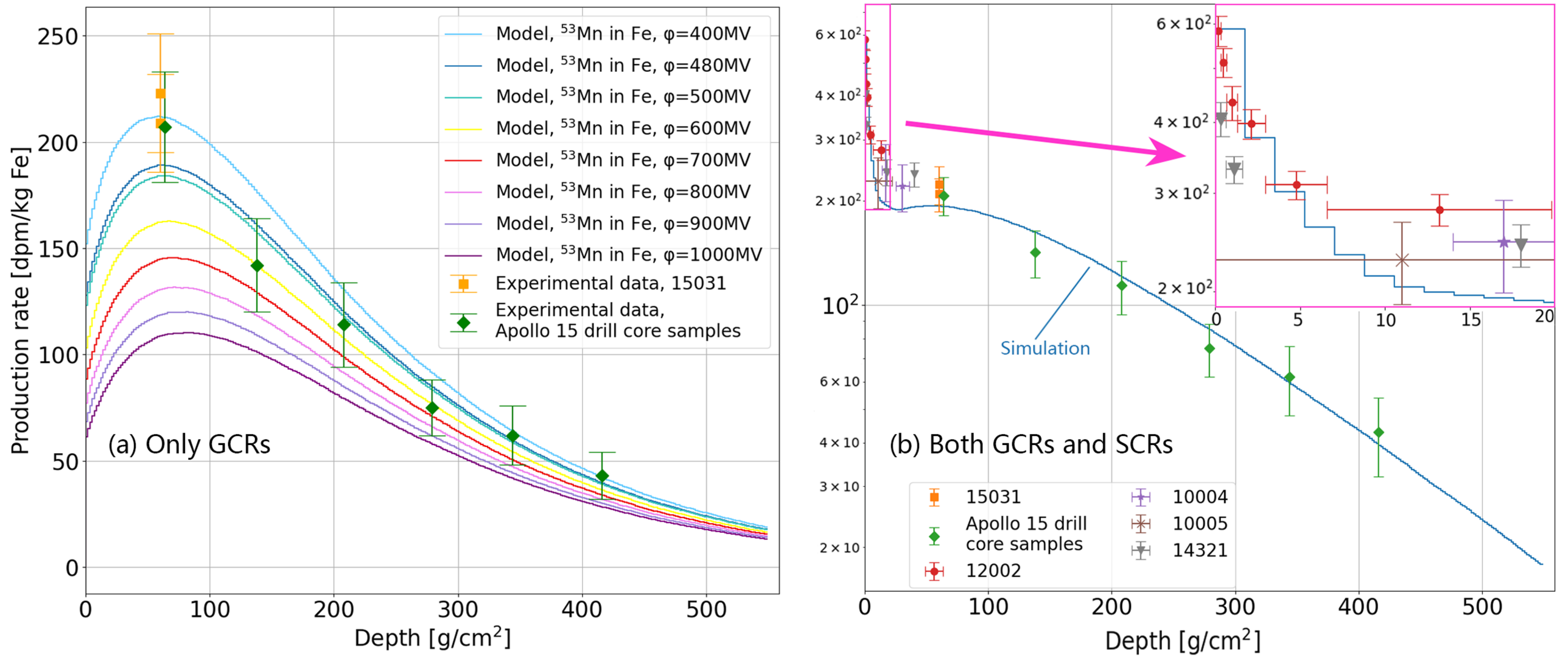
Model, ^{53}Mn in Fe, φ=400MV
Model, ^{53}Mn in Fe, φ=480MV
Model, ^{53}Mn in Fe, φ=500MV
Model, ^{53}Mn in Fe, φ=600MV
Model, ^{53}Mn in Fe, φ=700MV
Model, ^{53}Mn in Fe, φ=800MV
Model, ^{53}Mn in Fe, φ=900MV
Model, ^{53}Mn in Fe, φ=1000MV
Experimental data, 15031
Experimental data, Apollo 15 drill core samples
Production rate [dpm/kg Fe]
Depth [g/cm^2]
(a) Only GCRs
Simulation
(b) Both GCRs and SCRs
15031
Apollo 15 drill core samples
12002
10004
10005
14321

Figure 3.

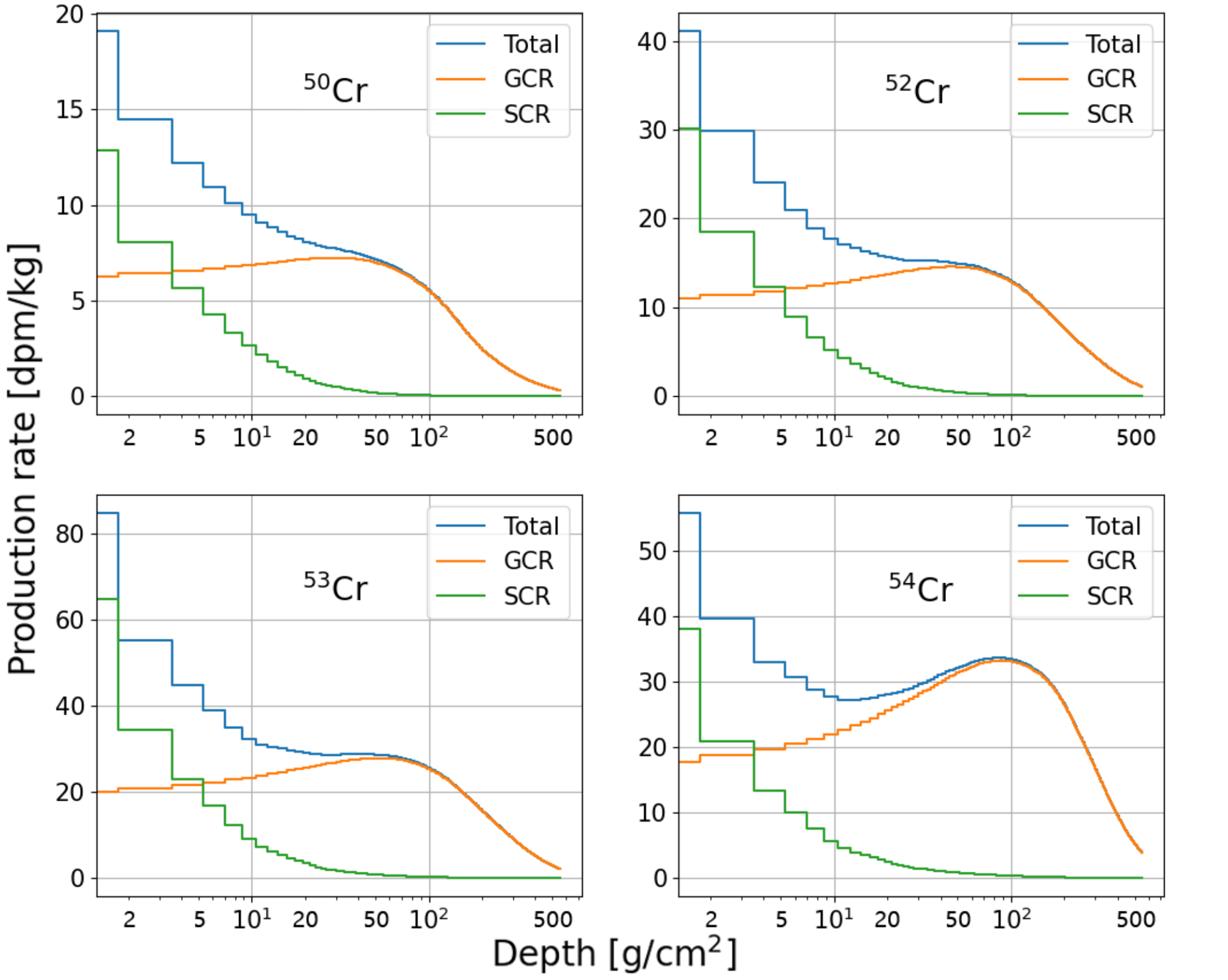
^{50}Cr
^{52}Cr
^{53}Cr
^{54}Cr
Total
GCR
SCR
Production rate [dpm/kg]
Depth [g/cm^2]
2
5
10^1
20
50
10^2
500

Figure 4.

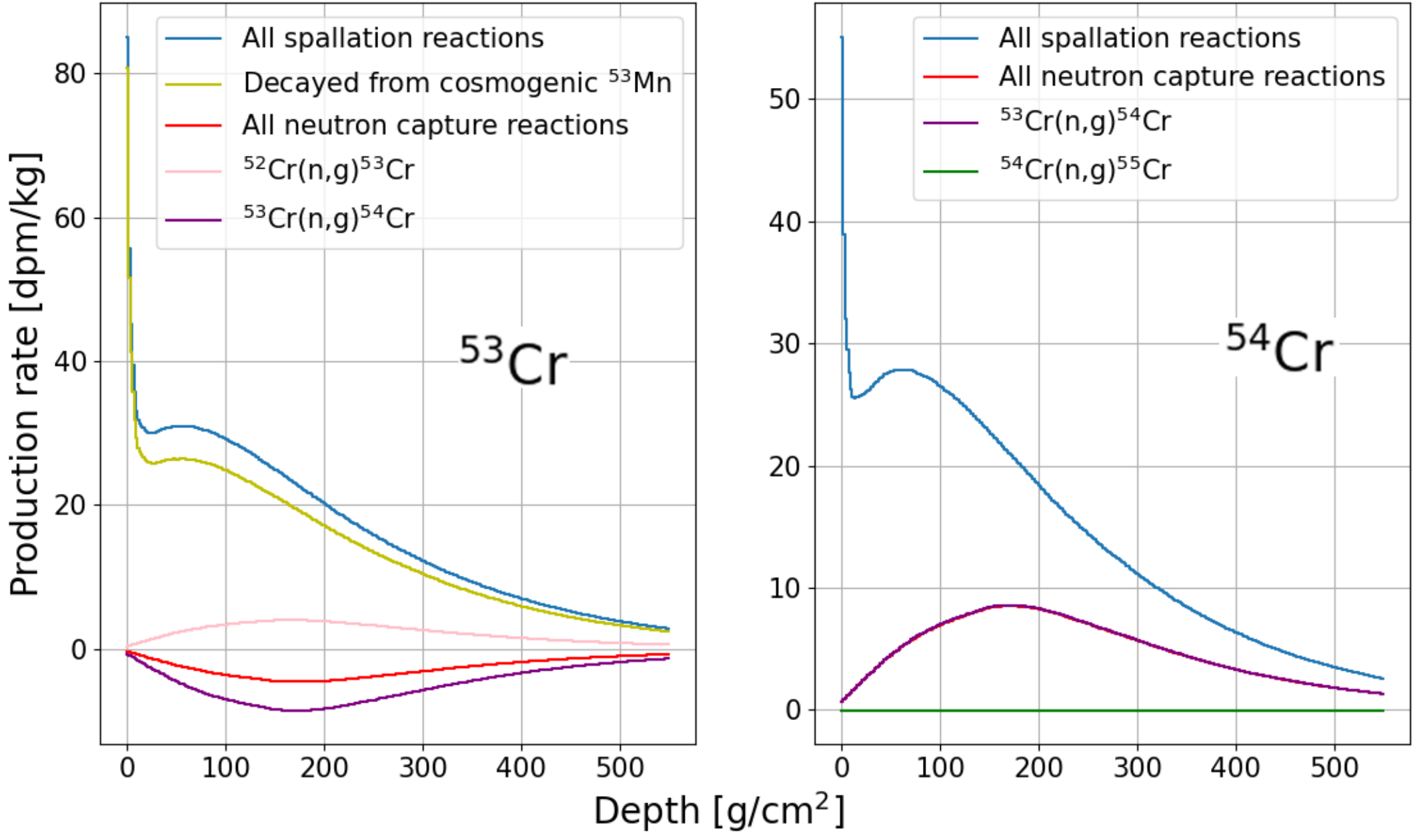
All spallation reactions
Decayed from cosmogenic ^{53}Mn
All neutron capture reactions
^{52}Cr(n,g)^{53}Cr
^{53}Cr(n,g)^{54}Cr
^{53}Cr
All spallation reactions
All neutron capture reactions
^{53}Cr(n,g)^{54}Cr
^{54}Cr(n,g)^{55}Cr
^{54}Cr
Production rate [dpm/kg]
Depth [g/cm^2]
0
20
40
60
80
100
200
300
400
500
10
30
50

Figure 5.

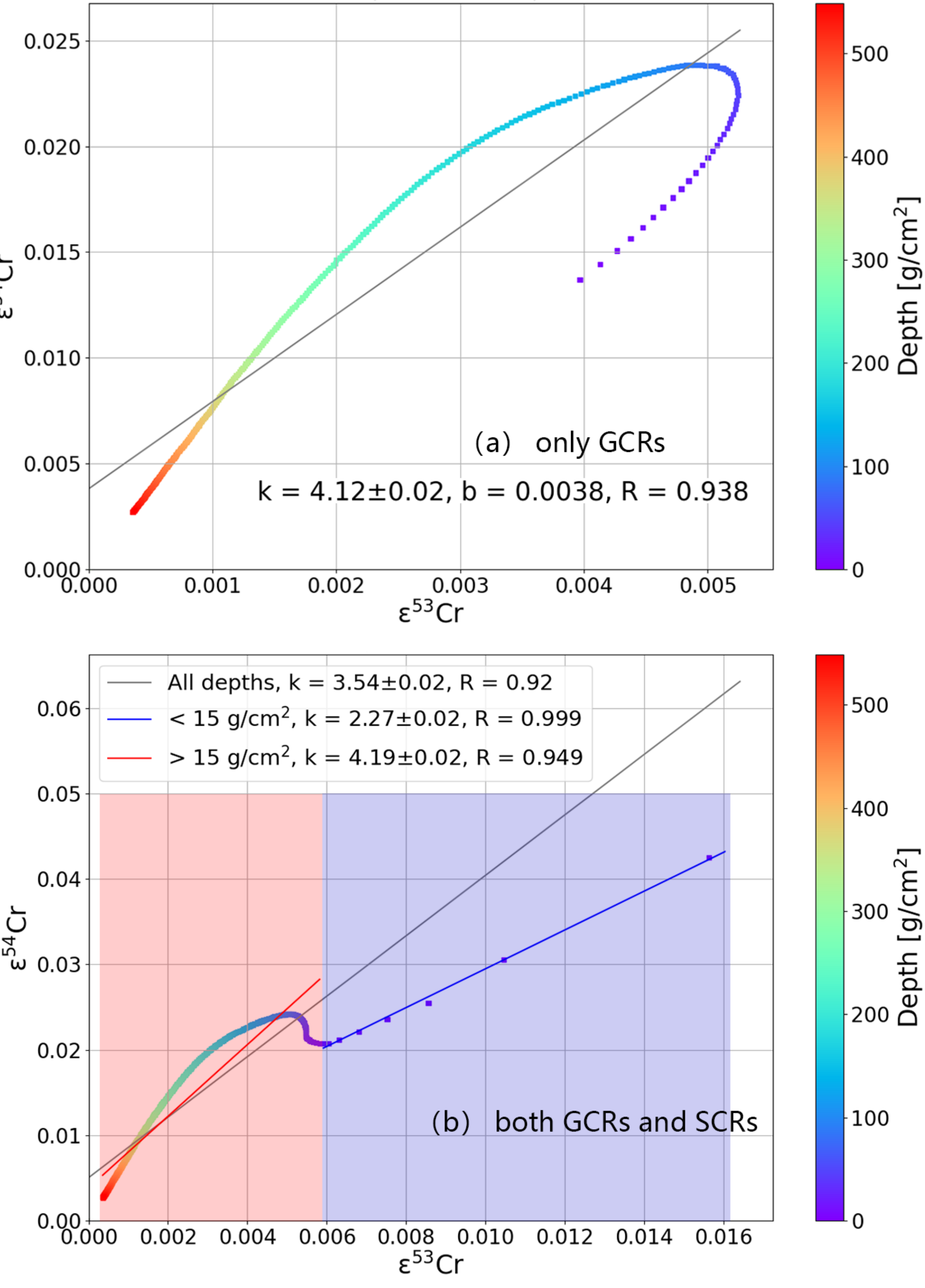
0.025
0.020
0.015
0.010
0.005
0.000
ε^{54}Cr
0.000
0.001
0.002
0.003
0.004
0.005
ε^{53}Cr
(a) only GCRs
k = 4.12±0.02, b = 0.0038, R = 0.938
500
400
300
200
100
0
Depth [g/cm^2]
All depths, k = 3.54±0.02, R = 0.92
< 15 g/cm^2, k = 2.27±0.02, R = 0.999
> 15 g/cm^2, k = 4.19±0.02, R = 0.949
0.06
0.05
0.04
0.03
0.02
0.01
0.00
ε^{54}Cr
0.000
0.002
0.004
0.006
0.008
0.010
0.012
0.014
0.016
ε^{53}Cr
(b) both GCRs and SCRs
500
400
300
200
100
0
Depth [g/cm^2]

Figure 6.

Slope of $\varepsilon^{53}Cr - \varepsilon^{54}Cr$

PCC

(a) Shallow region (< 15 g/cm^2)

(b) Deep region (> 15 g/cm^2)

Fe/Cr

Slope, 25 Myr
Slope, 50 Myr
Slope, 100 Myr
Slope, 500 Myr
PCC, 25 Myr
PCC, 50 Myr
PCC, 100 Myr
PCC, 500 Myr

Figure 7.

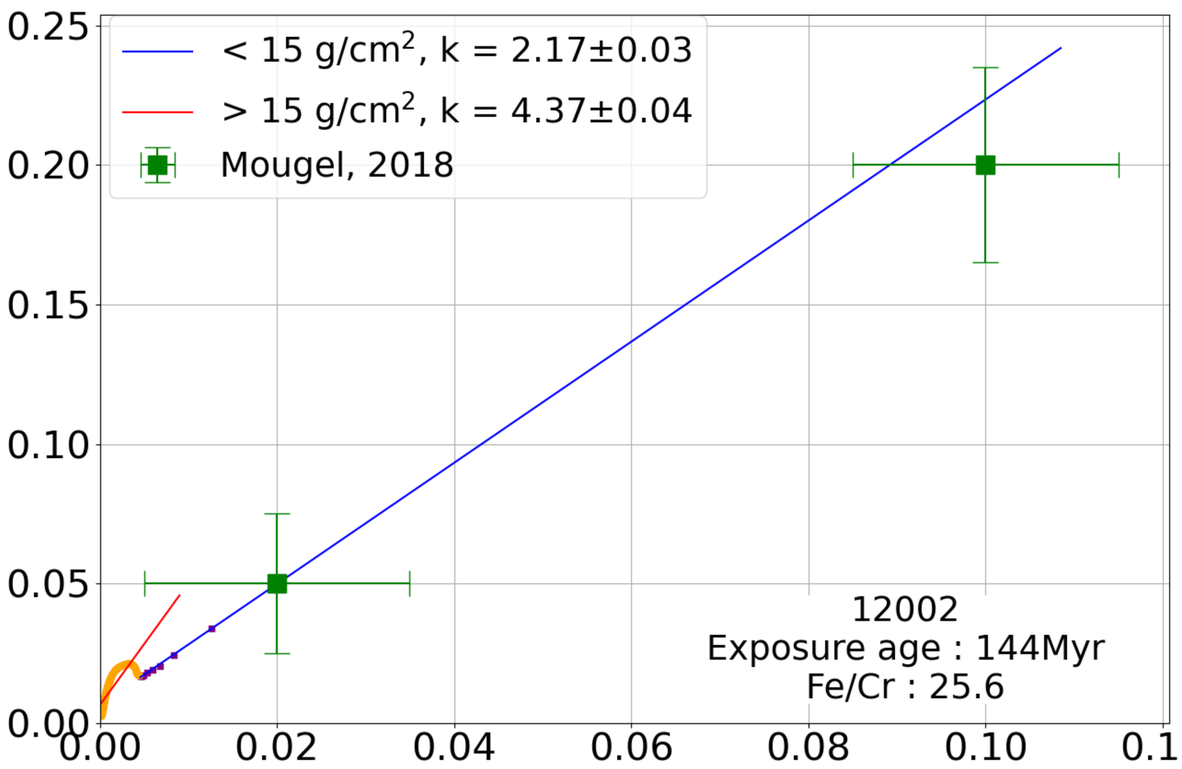

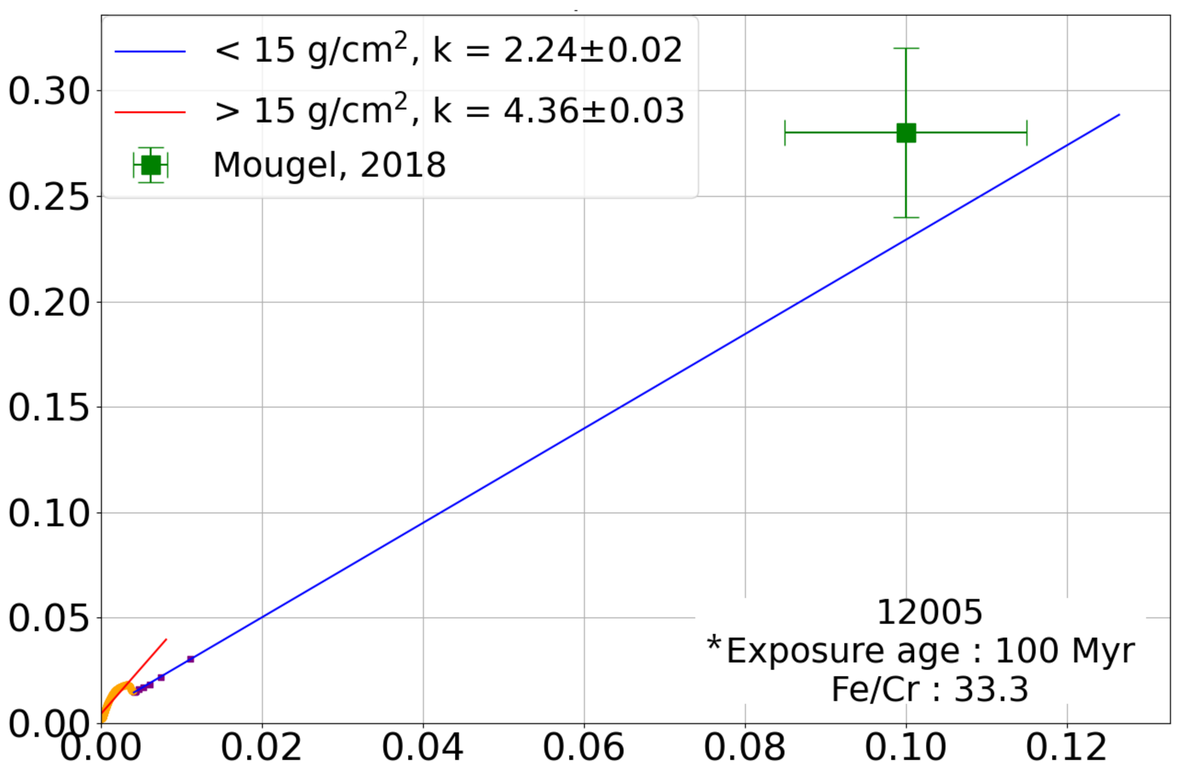

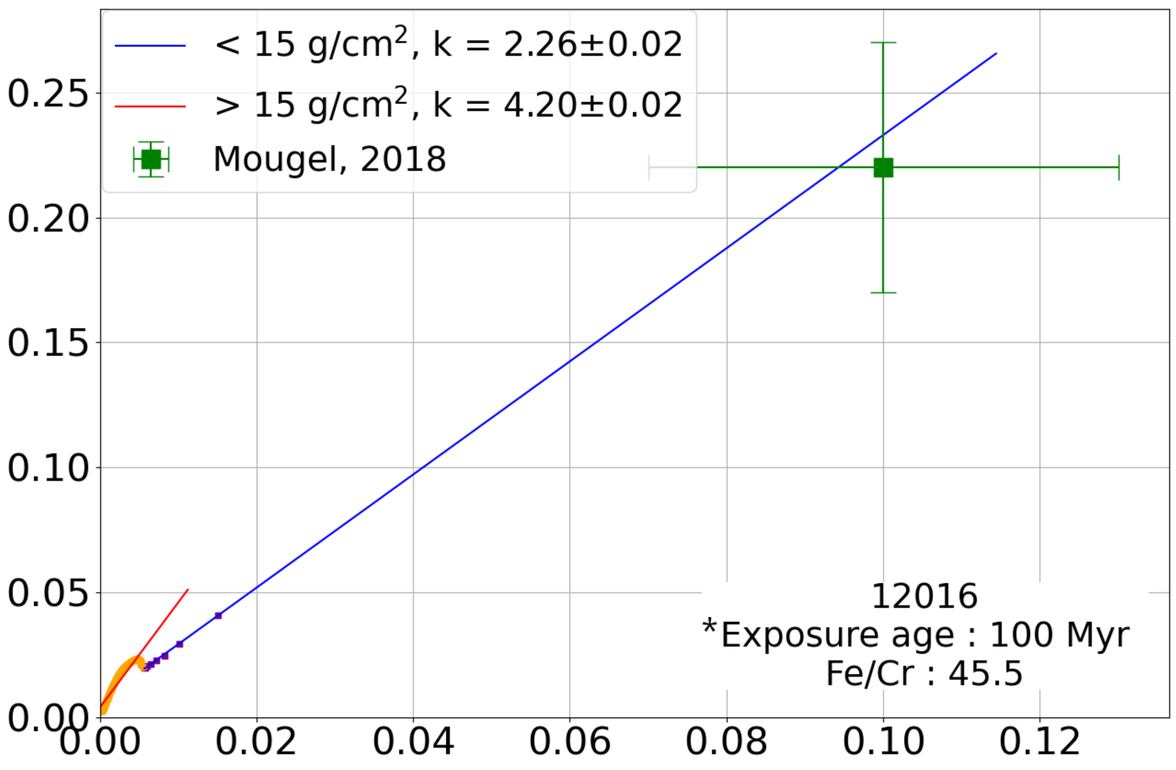

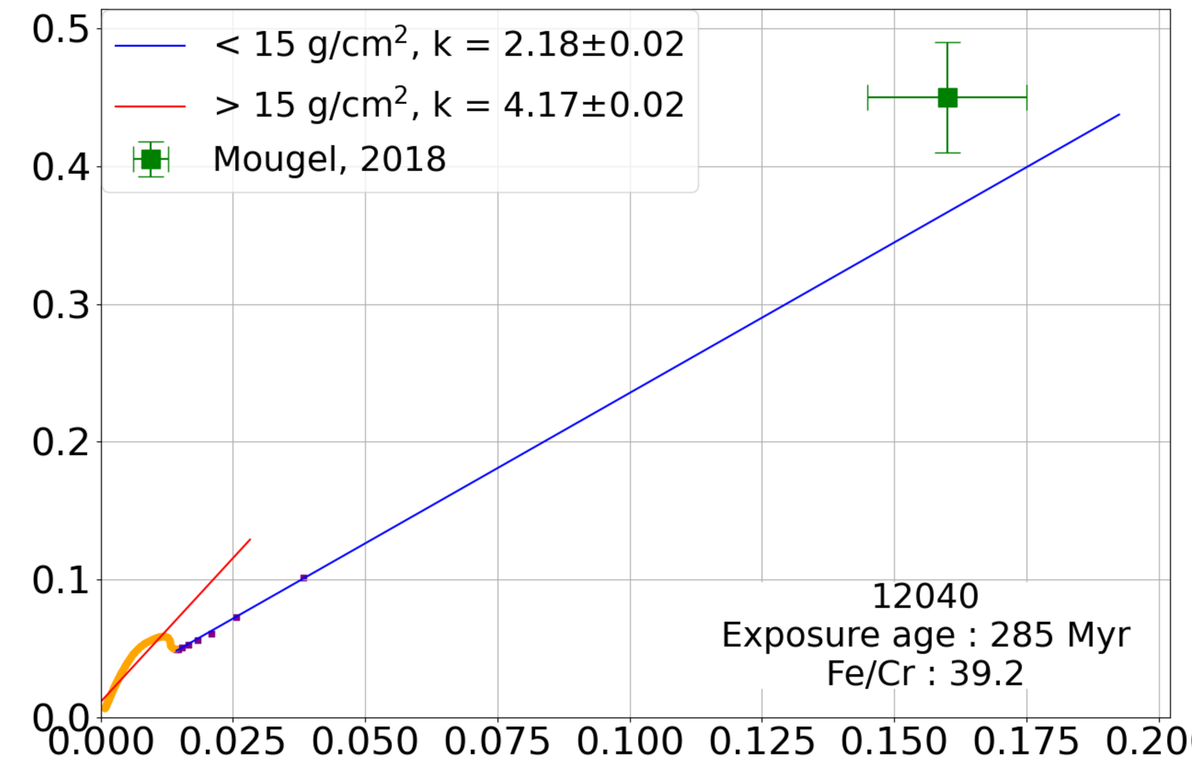

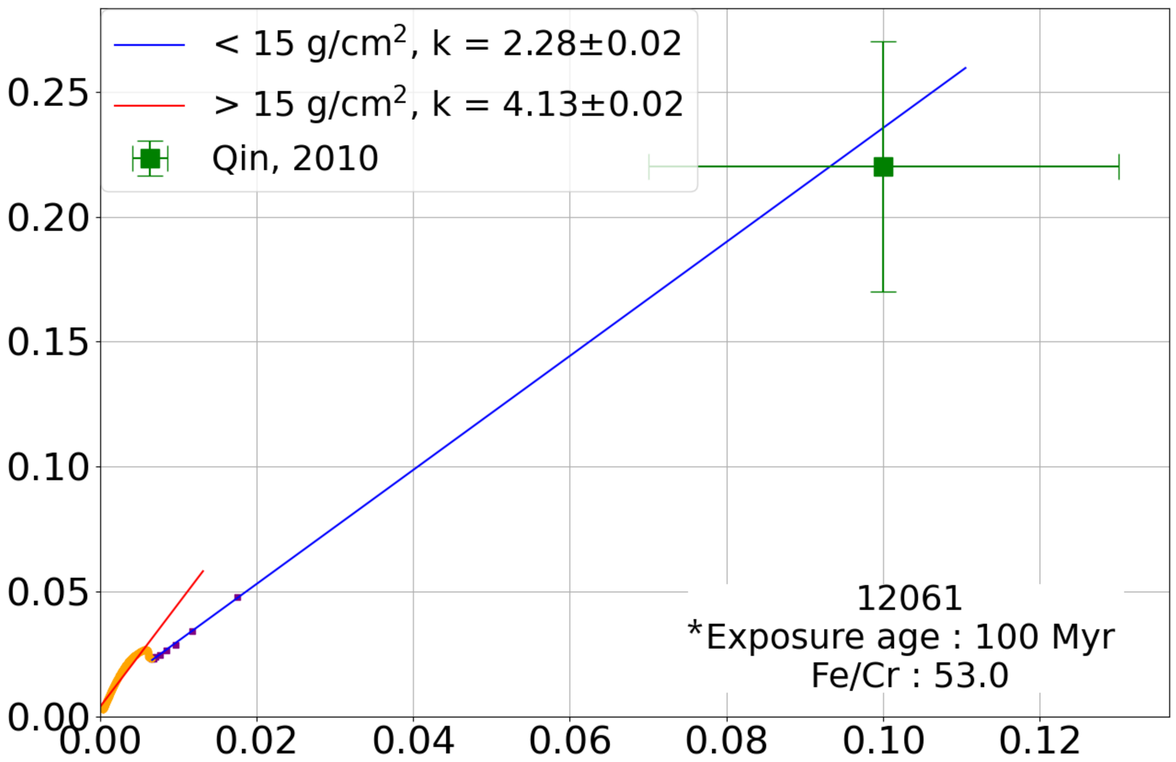

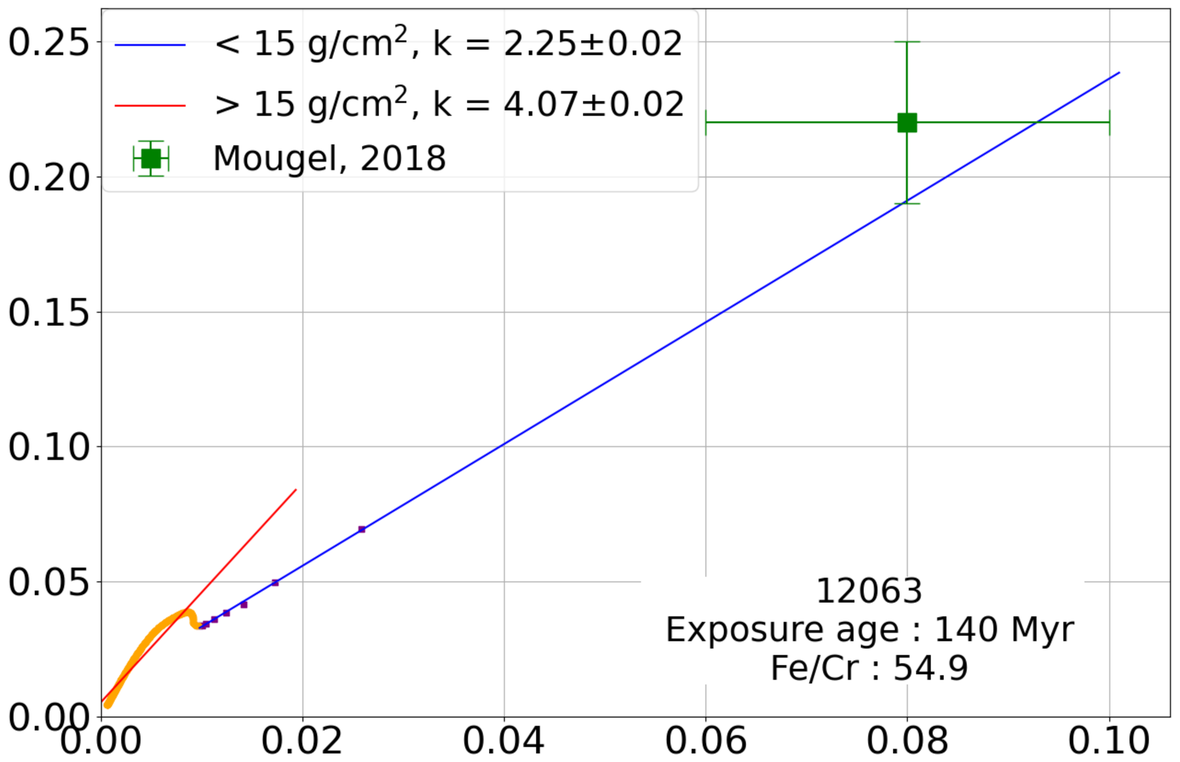

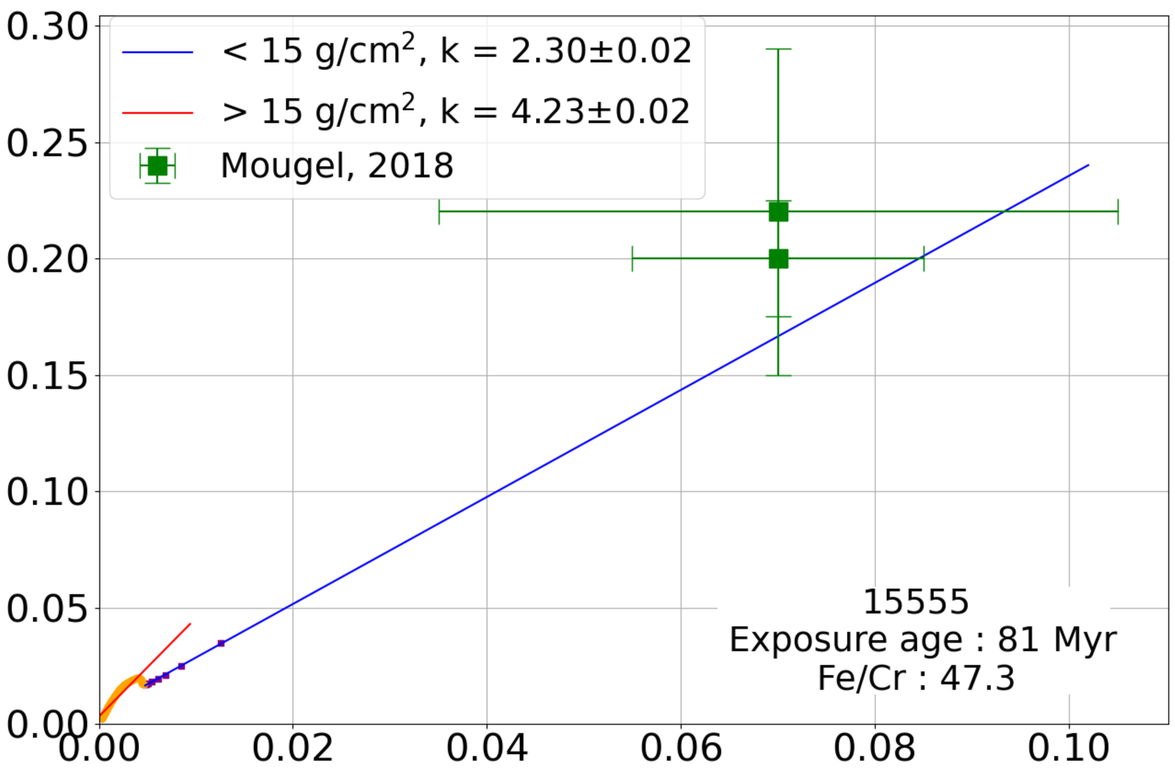

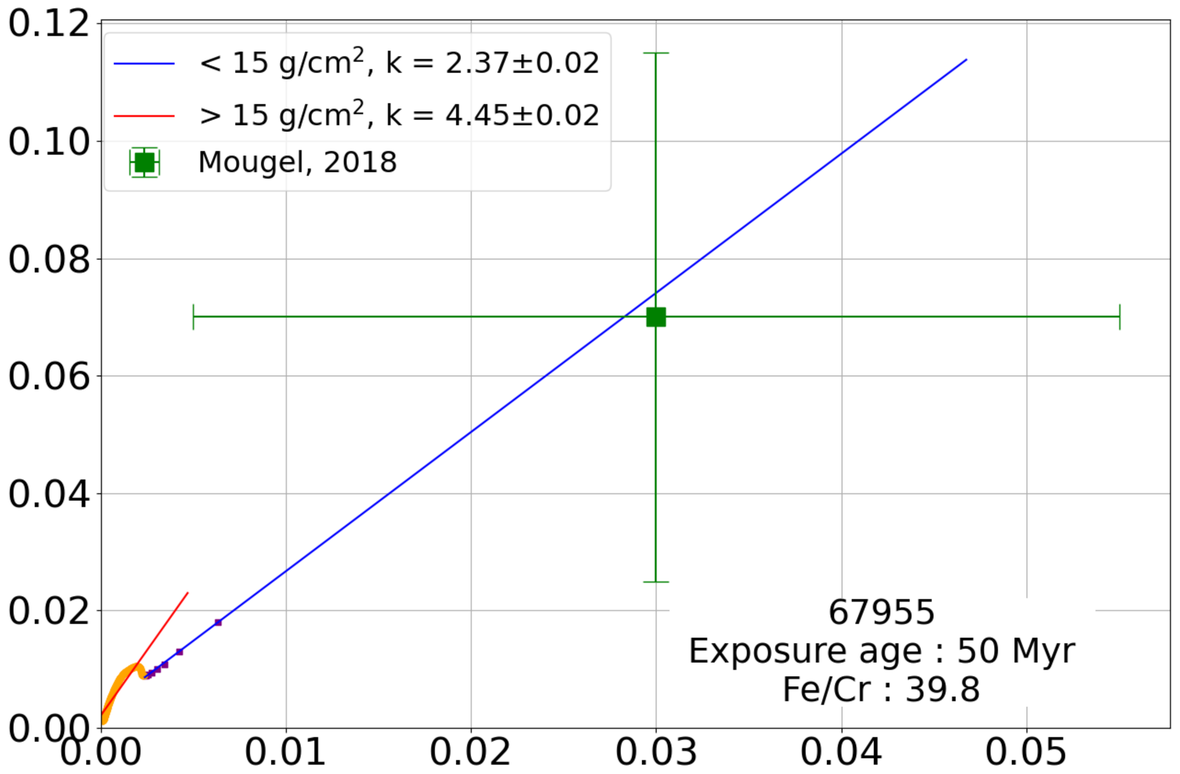

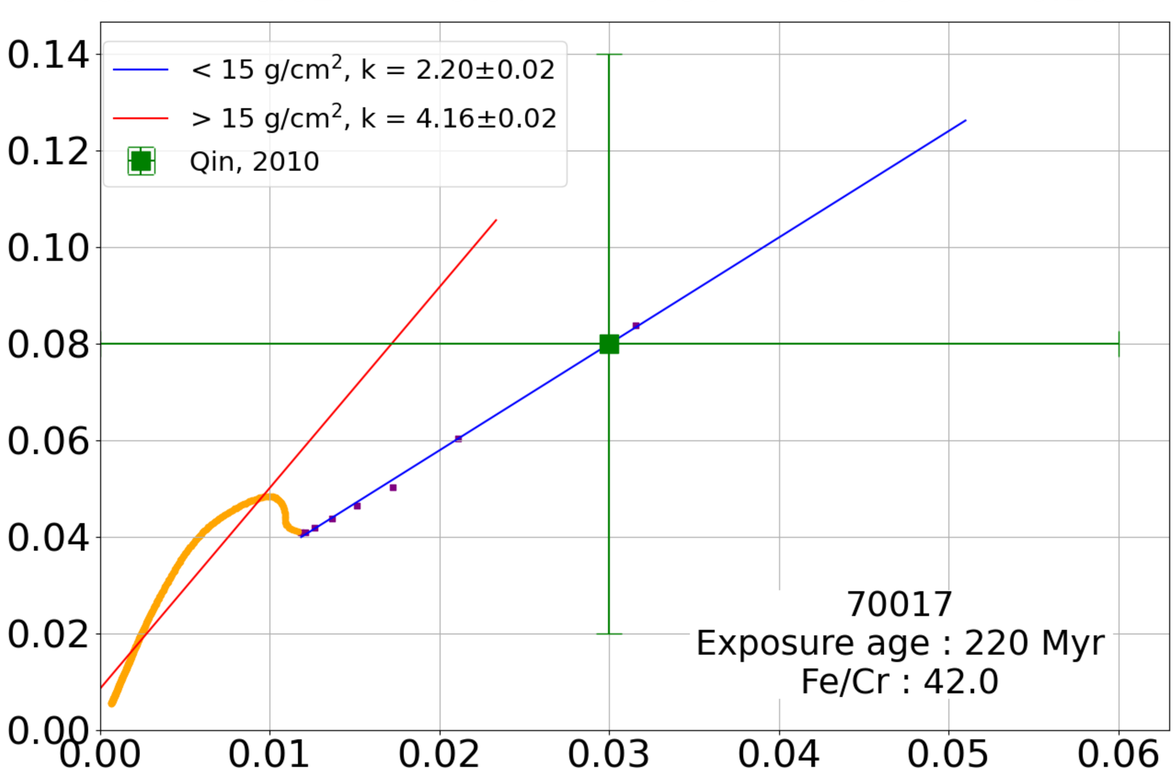

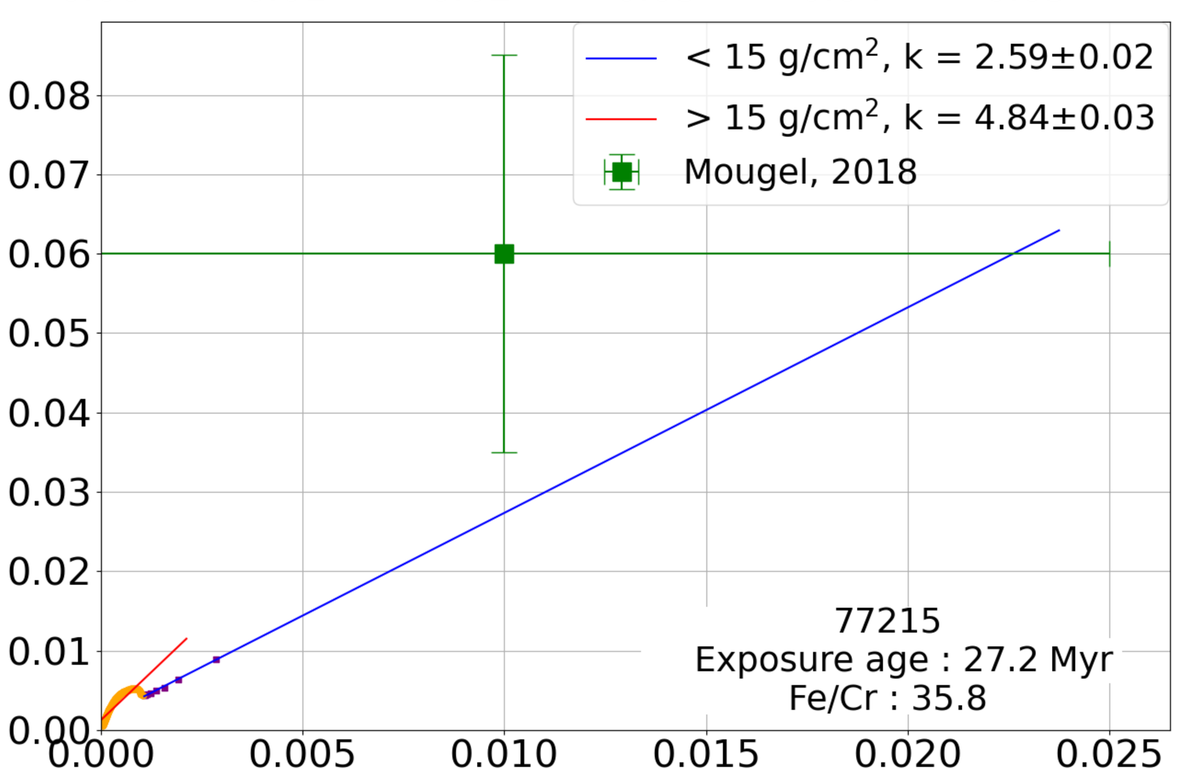

$\varepsilon^{54}Cr$

$\varepsilon^{53}Cr$

Figure 8.

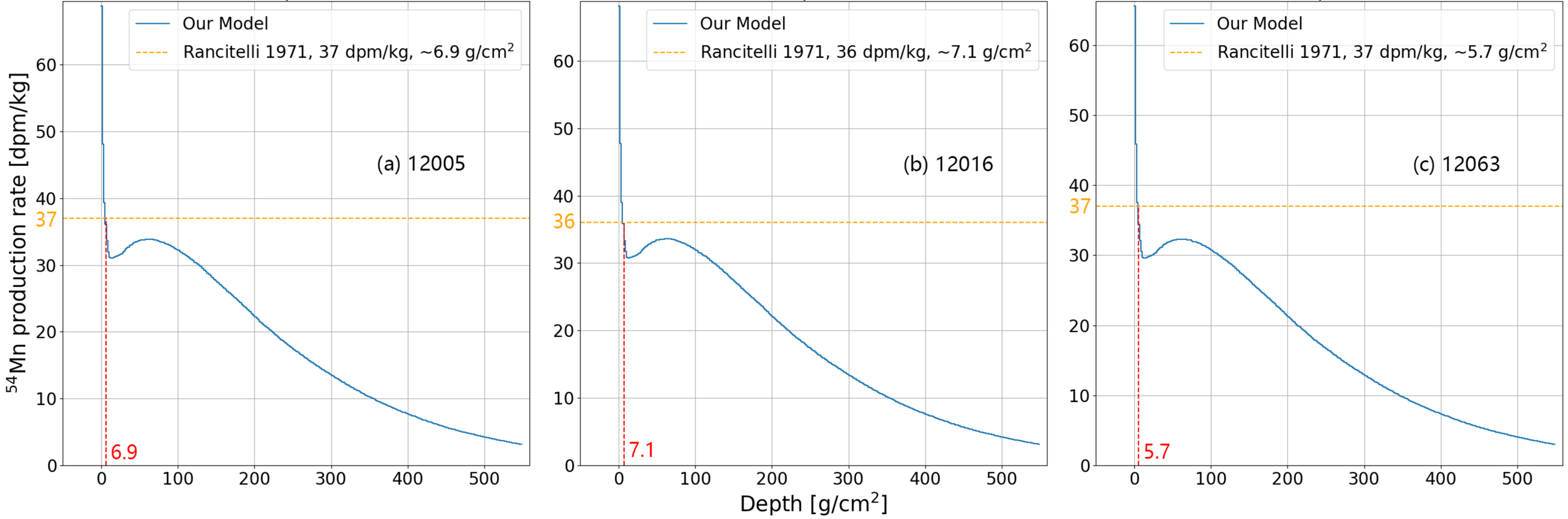
Our Model
Rancitelli 1971, 37 dpm/kg, ~6.9 g/cm^2
(a) 12005
37
6.9
Our Model
Rancitelli 1971, 36 dpm/kg, ~7.1 g/cm^2
(b) 12016
36
7.1
Our Model
Rancitelli 1971, 37 dpm/kg, ~5.7 g/cm^2
(c) 12063
37
5.7
^{54}Mn production rate [dpm/kg]
Depth [g/cm^2]